

# bradscholars

## Analytical and experimental investigations of dam-break flows in triangular channels with wet-bed conditions

Item Type	Article
Authors	Wang, B.;Liu, X.;Zhang, J.;Guo, Yakun;Chen, Y.;Peng, Y.;Liu, W.;Yang, S.;Zhang, F.
Citation	Wang B, Liu X, Zhang J et al (2020) Analytical and experimental investigations of dam-break flows in triangular channels with wet-bed conditions. ASCE Journal of Hydraulic Engineering. 146(10)
DOI	<a href="https://doi.org/10.1061/(ASCE)HY.1943-7900.0001808">https://doi.org/10.1061/(ASCE)HY.1943-7900.0001808</a>
Rights	(c) 2020 ASCE. Full-text reproduced in accordance with the publisher's self-archiving policy. This material may be downloaded for personal use only. Any other use requires prior permission of the American Society of Civil Engineers. This material may be found at <a href="https://doi.org/10.1061/(ASCE)HY.1943-7900.0001808">https://doi.org/10.1061/(ASCE)HY.1943-7900.0001808</a> .
Download date	2025-07-09 04:25:49
Link to Item	<a href="http://hdl.handle.net/10454/17840">http://hdl.handle.net/10454/17840</a>

# 1 Analytical and experimental investigations of dam-break flows in triangular 2 channels with wet-bed conditions

3 Bo Wang<sup>1</sup>, Xin Liu<sup>2</sup>, Jianmin Zhang<sup>3</sup>, Yakun Guo<sup>4</sup>, Yunliang Chen<sup>5</sup>, Yong Peng<sup>6</sup>, Wenjun Liu<sup>7</sup>, Sha  
4 Yang<sup>8</sup> and Fengjie Zhang<sup>9</sup>

5 <sup>1</sup>Professor, State Key Laboratory of Hydraulics and Mountain River Engineering, Sichuan University,  
6 Chengdu, 610065, China. E-mail: wangbo@scu.edu.cn

7 <sup>2</sup>Master's Candidate, State Key Laboratory of Hydraulics and Mountain River Engineering, Sichuan  
8 University, Chengdu, 610065, China. E-mail: 2078995580@qq.com

9 <sup>3</sup>Professor, State Key Laboratory of Hydraulics and Mountain River Engineering, Sichuan University,  
10 Chengdu, 610065, China. ORCID: <https://orcid.org/0000-0002-9154-231X>. E-mail:  
11 zhangjianmin@scu.edu.cn

12 <sup>4</sup>Professor, Faculty of Engineering & Informatics, University of Bradford, BD7 1DP, UK. E-mail:  
13 y.guo16@bradford.ac.uk

14 <sup>5</sup>Professor, State Key Laboratory of Hydraulics and Mountain River Engineering, Sichuan University,  
15 Chengdu, 610065, China. E-mail: 13541291332@163.com

16 <sup>6</sup>Associate Professor, State Key Laboratory of Hydraulics and Mountain River Engineering, Sichuan  
17 University, Chengdu, 610065, P. R. China. E-mail: pengyongscu@foxmail.com (Corresponding  
18 author)

19 <sup>7</sup>PhD student, State Key Laboratory of Hydraulics and Mountain River Engineering, Sichuan  
20 University, Chengdu, 610065, China. E-mail: liuwenjun\_scu@163.com

21 <sup>8</sup>Master's Candidate, State Key Laboratory of Hydraulics and Mountain River Engineering, Sichuan  
22 University, Chengdu, 610065, China. E-mail: ysha0919@163.com

23 <sup>9</sup>Master's Candidate, State Key Laboratory of Hydraulics and Mountain River Engineering, Sichuan  
24 University, Chengdu, 610065, China. E-mail: 1114139373@qq.com

25 **Abstract:** Based on the method of characteristics, an analytical solution for the

26 one-dimensional shallow-water equations is developed to simulate the instantaneous dam-break  
27 flows propagating down a triangular wet bed channel in this study. The internal relationships  
28 between the hydraulic properties associated with the dam-break flow are investigated through the  
29 comparisons with the well-known analytical solutions for rectangular channels. Meanwhile,  
30 laboratory experiments are conducted in a prismatic, horizontal and smooth flume with a triangular  
31 cross-section. The non-intrusive digital image processing is applied for obtaining water surface  
32 profiles and stage hydrographs. Results show that the dam-break flow propagation depends on the  
33 dimensionless parameter  $h_d^*$  defined as the ratio of initial tailwater depth over reservoir head.  $h_d^*$   
34 has significant effect on the dam-break wave in the downstream flooded area. For  $h_d^* \leq 0.4$ , the  
35 water surface profiles in the reservoir for different  $h_d^*$  at a given time remains similar. For  $h_d^* \geq$   
36 0.5, extra negative waves occur in the reservoir, leading to the water surface undulations. Undular  
37 bores are generated at the dam site and propagate downstream. Time evolution of dam-break flows  
38 under three different reservoir heads is similar for the same  $h_d^*$ . The inception of water surface  
39 profile change is earlier when the reservoir head is larger. The analytical model shows satisfactory  
40 agreement with the experimental results though some errors exist between the analytical solution and  
41 measurements due to the formation of extra negative waves, jet and undular bores. The similarities  
42 and discrepancies between the hydraulics in the triangular and rectangular channels are identified  
43 analytically in terms of the profiles of water depth, velocity, discharge, bore height and wave-front  
44 celerity with  $h_d^*$ . The presented solution could be applied to predict the effect of wet bed condition  
45 on the dam-break wave in triangular channels, while laboratory measurement data could be used for  
46 validating analytical and numerical models.

47 **Keywords:** Dam-break wave; Triangular channel; Wet bed; Analytical solution; Digital image  
48 processing.

49

## 50 **Introduction**

51 The losses of both properties and human lives caused by dam-break flood wave are considerable,  
52 which continuously drives the study of dam-break wave in order to better understand its propagation  
53 characteristics for issuing timely flood warning. The investigation on dam-break waves is extremely  
54 vital in providing the information for flood risk assessment and for both hazard classification and  
55 emergency planning, particularly when the dam is located upstream of heavily populated and  
56 industrialized areas. The propagation of dam-break flood waves strongly depends on the  
57 cross-sectional shape of river (Su and Barnes 1970; Sakkas and Strelkoff 1973, 1976; Katopodes and  
58 Strelkoff 1978; Katopodes and Schamber 1983; Schamber and Katopodes 1984; Wu et al. 1993,  
59 1999; Zanuttigh and Lamberti 2011; Wang et al. 2017). For the sake of convenience, the wide and  
60 shallow cross section of rivers is often conceptualized as a rectangle; while the narrow and deep  
61 cross section usually is simplified as a triangle.

62 Due to its practical importance and theoretical interests, extensive studies have been conducted  
63 to investigate the dam-break flows in rectangular channels using both the theoretical analysis and  
64 laboratory experiments. Ritter (1892) could be considered as the pioneer in dam-break flow study  
65 who derived an analytical solution for the hydrodynamic problem of instantaneous dam-break flow  
66 in a frictionless and horizontal rectangular channel. Since then, many well-known analytical studies  
67 of the dam break have been conducted (Dressler 1952; Whitham 1955; Stoker 1957; Hunt 1982,  
68 1983, 1984; Mangeney et al. 2000; Fernandez-Feria 2006; Hogg 2006; Ancy et al. 2008; Chanson

69 2009; and Wang et al. 2020a). In addition to analytical study, laboratory experiment is also a popular  
70 method for investigating the dam-break flows propagating along the rectangular channel (Dressler  
71 1954; Miller and Chaudhry 1989; Bellos et al. 1992; Fraccarollo and Toro 1995; Lauber and Hager  
72 1998a, b; Stansby et al. 1998; Bukreev and Gusev 2005; Soares-Frazão and Zech 2007;  
73 Ozmen-Cagatay and Kocaman 2010; Ozmen-Cagatay and Kocaman 2012; Oertel and Bung 2012;  
74 Chen et al. 2013; LaRocque et al. 2013; Ozmen-Cagatay et al. 2014; Kocaman and Ozmen-Cagatay  
75 2015; Liu et al. 2018; Liu et al. 2019; Wang et al. 2019; and Wang et al. 2020b).

76 Comparing with the extensive studies of dam break flow propagating along rectangular  
77 channel, few studies are carried out to investigate the dam-break waves in triangular channels with a  
78 wet bed. Sakkas and Strelkoff (1973) analyzed the hydraulics of dam-break floods in a triangular  
79 channel with a dry bed. Zanuttigh and Lamberti (2011) highlighted the effect of cross-sectional shape  
80 on dam-break wave propagation along channels and presented the celerity, velocity, and bore speed  
81 for triangular channels as functions of the relative flow depth difference. An analytical solution for  
82 the water surface profiles of dam-break flows in a triangular channel can be obtained through the  
83 simplification of the theoretical approach proposed by Wu et al. (1999) for the channel of a  
84 trapezoidal cross section. Using the method of Blasius similarity, Chen et al. (2011) obtained  
85 analytical solutions which were the same as those of Wu et al. (1999). These analytical solutions are  
86 verified by laboratory measurements in a triangular channel with a dry bed conducted by Chen et al.  
87 (2011). On the one hand, although the aforementioned analytical models (i.e., Sakkas and Strelkoff  
88 1973; Wu et al. 1999; Zanuttigh and Lamberti 2011; Chen et al. 2011) for dam-break flows in  
89 triangular channels were developed by researchers using different approaches, the internal  
90 relationships among the hydraulic parameters associated with this phenomenon have not been

91 appropriately discussed. Moreover, the applicability of analytical solutions remains unknown due to  
92 the lack of laboratory data for verification. On the other hand, the effect of wet-bed conditions on the  
93 dam-break wave propagation along a triangular channel is poorly understood. Laboratory experiment  
94 on the dam-break flow on wet bed with a triangular cross section is required to provide flow features  
95 as well as validate analytical solutions. To the authors' best knowledge, few experimental studies  
96 have been carried out to investigate the dam-break flows in a triangular channel with a wet bed.

97 The main objectives of the present study are: (1) to develop analytical solutions of the  
98 one-dimensional shallow-water equations for dam-break flows in a triangular channel using the  
99 method of characteristics; (2) to collect data on the spatial-temporal evolution of water surface at  
100 upstream and downstream of the dam using digital image processing; (3) to evaluate the effect of wet  
101 bed condition on the dam-break wave propagation along the channel using both the analytical and  
102 physical models; and (4) to validate analytical solutions with the accompanying experiments.

103

#### 104 **Analytical Model**

105 For an infinitely long horizontal channel of a uniform cross-section, the rarefaction wave and shock  
106 wave (or bore) generated by an instantaneous dam break over wet bed is shown in Fig. 1. The  
107 structure of the dam-break flow, which is used widely in the development of analytical solutions  
108 (Stoker 1957; Wu et al. 1999; Zanuttigh and Lamberti 2011; Wang et al. 2020a), can be divided into  
109 four zones down a channel. Zone 1 is the undisturbed water far upstream with reservoir head being  
110 equal to  $h_u$  and velocity  $u_u = 0$ . In Zone 2, the rarefaction wave propagates upstream connecting Zone  
111 1 with Section  $M-M$  (i.e., rarefaction wave front, or called negative wave front) and downstream  
112 connecting Zone 3 with Section  $N-N$  (i.e., rarefaction wave tail). Zone 3 has a constant velocity and

113 depth (i.e.,  $u_c$  and  $h_c$ ) that connects the shock wave (Section  $R-R$ ). Zone 4 is the downstream region  
 114 with a tailwater depth of  $h_d$  and velocity  $u_d = 0$ , limited upstream by the shock wave that travels with  
 115 a constant speed  $\xi$ .

116

### 117 ***One-dimensional Equations for Arbitrary Channel Section***

118 The propagation of a dam-break flood resulting from a sudden release of a mass fluid in a channel is  
 119 governed by the equations of gradually varied unsteady flow in an open channel, the  
 120 one-dimensional (1D) shallow-water equations (Chow 1959). For an infinitely long prismatic and  
 121 horizontal channel, if the effect of friction is neglected, the equations can be written as:

$$122 \quad \frac{\partial h}{\partial t} + u \frac{\partial h}{\partial x} + \frac{A}{B} \frac{\partial u}{\partial x} = 0 \quad (1)$$

$$123 \quad \frac{\partial u}{\partial t} + u \frac{\partial u}{\partial x} + g \frac{\partial h}{\partial x} = 0 \quad (2)$$

124 where  $h$  = flow depth,  $x$  = distance,  $t$  = time,  $g$  = gravity acceleration,  $u$  = mean flow velocity,  $B$  =  
 125 water surface width,  $A$  = cross-sectional area.

126 The initial conditions of the dam-break problem considered in this study can be described by

$$127 \quad u|_{t=0} = 0, \quad h|_{t=0} = \begin{cases} h_u & x < 0 \\ h_d & x > 0 \end{cases} \quad (3)$$

128 where subscripts " $u$ " and " $d$ " = undisturbed far upstream reach and quiet zone downstream,  
 129 respectively.

130 The method of characteristics is usually used to solve the system of partial differential  
 131 equations composed of Eqs. (1–2) which yields a characteristic system of equations:

$$132 \quad \frac{d}{dt} \left( u + \int_0^h \sqrt{g \frac{B}{A}} d\eta \right) = 0 \quad \text{along} \quad \frac{dx}{dt} = u + \sqrt{g \frac{A}{B}} \quad (4)$$

133 
$$\frac{d}{dt} \left( u - \int_0^h \sqrt{g \frac{B}{A}} d\eta \right) = 0 \quad \text{along} \quad \frac{dx}{dt} = u - \sqrt{g \frac{A}{B}} \quad (5)$$

134 where  $\int_0^h \sqrt{g \frac{B}{A}} d\eta =$  Escoffier stage variable (Escoffier 1962; Henderson 1966; Schamber and  
 135 Katopodes 1984; Wu et al. 1999; Aureli et al. 2014).

136 Along the forward characteristics, there is

137 
$$\left( u + \int_0^h \sqrt{g \frac{B}{A}} d\eta \right) - \left( u_u + \int_0^{h_u} \sqrt{g \frac{B}{A}} d\eta \right) = 0 \quad (6)$$

138 Applying the condition  $u_u = 0$  in Eq. (6) yields

139 
$$u = \int_0^{h_u} \sqrt{g \frac{B}{A}} d\eta - \int_0^h \sqrt{g \frac{B}{A}} d\eta \quad (7)$$

140 Since each of the backward characteristics is a straight line,  $dx/dt$  can be replaced by  $x/t$  for an  
 141 infinitely long prismatic channel. Eq. (5) can be transformed as

142 
$$\frac{x}{t} = u - \sqrt{g \frac{A}{B}} \quad (8)$$

143 Substituting Eq. (7) into Eq. (8) yields

144 
$$\int_0^h \sqrt{\frac{B}{A}} d\eta + \sqrt{\frac{A}{B}} = \int_0^{h_u} \sqrt{\frac{B}{A}} d\eta - \frac{x}{t\sqrt{g}} \quad (9)$$

145 The motion of the shock wave is described by the Rankine-Hugoniot equations for mass and  
 146 momentum:

147 
$$\xi = \frac{A_c u_c - A_d u_d}{A_c - A_d} \quad (10)$$

148 
$$u_c = u_d + \left[ g \frac{(A_c \bar{h}_c - A_d \bar{h}_d)(A_c - A_d)}{A_c A_d} \right]^{1/2} \quad (11)$$

149 where subscript "c" = back reach of the shock;  $\bar{h}$  = centroid depth for the cross section;  $\xi =$   
 150 propagation velocity of the shock, so-called shock wave-front celerity, and defined by

151 
$$\xi = \frac{dx_R}{dt} \quad (12)$$

152 in which  $x_R$  = shock location shown in Fig. 1, as a function of time  $t$ .

153 Eq. (10–11) can be simplified by applying the condition  $u_d = 0$  as:

154 
$$\xi = \frac{A_c u_c}{A_c - A_d} \quad (13)$$

155 
$$u_c = \left[ g \frac{(A_c \bar{h}_c - A_d \bar{h}_d)(A_c - A_d)}{A_c A_d} \right]^{1/2} \quad (14)$$

156 The hydraulic characteristics, i.e., flow depth and velocity, are unique in the cross section  $N-N$   
 157 connecting the Zones 2 and 3. Applying Eq. (4) in this boundary condition yields the flow velocity in  
 158 the Zone 3:

159 
$$u_c = \int_0^{h_u} \sqrt{g \frac{B}{A}} d\eta - \int_0^{h_c} \sqrt{g \frac{B}{A}} d\eta \quad (1$$

160 
$$5)$$

161 Substituting Eq. (14) into Eq. (15) yields the flow velocity:

162 
$$\int_0^{h_u} \sqrt{\frac{B}{A}} d\eta - \int_0^{h_c} \sqrt{\frac{B}{A}} d\eta = \left[ \frac{(A_c \bar{h}_c - A_d \bar{h}_d)(A_c - A_d)}{A_c A_d} \right]^{1/2} \quad (16)$$

163 Eqs. (9) and (16) are applicable for a prismatic channel with arbitrary cross-sections.

164

165 ***Analytical Solutions for Triangular Channels***

166 For a triangular channel, the cross-sectional area is half of the product of the flow depth and the

167 water surface width. Applying this condition for the rarefaction wave, Eq. (9) can be simplified as:

168 
$$\int_0^h \sqrt{\frac{2}{h}} d\eta + \sqrt{\frac{h}{2}} = \int_0^{h_u} \sqrt{\frac{2}{h}} d\eta - \frac{x}{t\sqrt{g}} \quad (17)$$

169 Integrating Eq. (17) yields the dimensionless flow depth

170 
$$h^* = \frac{h}{h_u} = \frac{4}{25} \left( 2 - \frac{x}{t\sqrt{2gh_u}} \right)^2 \quad (18)$$

171 Let

172 
$$\frac{x}{t\sqrt{2gh_u}} = \frac{X}{T} \quad (19)$$

173 where  $X$  = dimensionless distance from the dam site,  $X = x/h_u$ ; and  $T$  = dimensionless time,  $T =$

174  $t(g/h_u)^{1/2}$ . A simplified form of Eq. (18) can be obtained as:

175 
$$h^* = \frac{2}{25} \left( 2\sqrt{2} - \frac{X}{T} \right)^2 \quad (20)$$

176 Let  $h^* = 1$ , the dimensionless location and celerity of the negative wave front are obtained as:

177 
$$X_M = C_1^* T \quad (21)$$

178 
$$C_1^* = -\frac{\sqrt{2}}{2} \quad (22)$$

179 Applying Eq. (20) in Eq. (8) yields the dimensionless velocity:

180 
$$u^* = \frac{u}{\sqrt{gh_u}} = \frac{2}{5} \left( \sqrt{2} + 2\frac{X}{T} \right) \quad (23)$$

181 The dimensionless discharge is expressed as:

182 
$$Q^* = \frac{Q}{A_u \sqrt{gh_u}} = \frac{Au}{A_u \sqrt{gh_u}} \quad (24)$$

183 For a triangular channel, the cross sections of the Zones (1) and (2) are similar triangles. The

184 area ratio of the cross sections is equal to the square of the ratio of the corresponding flow depth:

185 
$$\frac{A}{A_u} = \left( \frac{h}{h_u} \right)^2 \quad (25)$$

186 The dimensionless discharge and the Froude Number are obtained from Eqs. (20, 23–25) as:

187 
$$Q^* = \left( \frac{h}{h_u} \right)^2 \cdot \frac{u}{\sqrt{gh_u}} = \frac{4}{3125} \left( 2\sqrt{2} - \frac{X}{T} \right)^4 \left( 2\sqrt{2} + 4\frac{X}{T} \right) \quad (26)$$

188 
$$F_r = \frac{2\left(1 + \sqrt{2} \frac{X}{T}\right)}{2\sqrt{2} - \frac{X}{T}} \quad (27)$$

189 For a triangular channel, the centroid depth for the cross section is one third of the flow depth.

190 Applying this condition for the shock wave, Eq. (16) can be simplified as:

191 
$$\int_0^{h_u} \sqrt{\frac{2}{h}} d\eta - \int_0^{h_c} \sqrt{\frac{2}{h}} d\eta = \left[ \frac{1}{3} \left( \frac{A_c}{A_d} h_c - h_c - h_d + \frac{A_d}{A_c} h_d \right) \right]^{1/2} \quad (28)$$

192 Applying the condition that the cross-sectional area of triangular channels is proportional to  
 193 the square of the depth in the Zones (3) and (4), Eq. (28) is transformed as:

194 
$$\int_0^{h_u} \sqrt{\frac{2}{h}} d\eta - \int_0^{h_c} \sqrt{\frac{2}{h}} d\eta = \left[ \frac{1}{3} \left( \frac{h_c^3}{h_d^2} - h_c - h_d + \frac{h_d^3}{h_c^2} \right) \right]^{1/2} \quad (29)$$

195 Integrating Eq. (29) yields:

196 
$$\left(h_c^*\right)^5 - 25\left(h_d^*\right)^2 \left(h_c^*\right)^3 + 48\left(h_d^*\right)^2 \left(h_c^*\right)^{\frac{5}{2}} - \left(h_d^* + 24\right) \left(h_d^*\right)^2 \left(h_c^*\right)^2 + \left(h_d^*\right)^5 = 0 \quad (30)$$

197 where  $h_c^* = h_c / h_u$  = dimensionless water depth in the reach upstream of the shock and  $h_d^* = h_d / h_u$  =  
 198 dimensionless tailwater depth.

199 The hydraulic characteristic of the Zone 2 is the same as that of the Zone 3 at the junction  $N-N$   
 200 (i.e., rarefaction wave tail). Applying Eqs. (19) and (20) in the junction cross section yields the  
 201 dimensionless depth and velocity, respectively:

202 
$$h_c^* = \frac{2}{25} \left( 2\sqrt{2} - \frac{X_N}{T} \right)^2 \quad (31)$$

203 
$$u_c^* = \frac{u_c}{\sqrt{gh_u}} = \frac{2}{5} \left( \sqrt{2} + 2 \frac{X_N}{T} \right) \quad (32)$$

204 where the subscript "N" refers to the junction  $N-N$ , and  $X_N$  is defined by:

205 
$$X_N = \frac{x_N}{h_u} \quad (3)$$

206 3)

207 Applying Eq. (31) in Eq. (32) yields:

$$208 \quad u_c^* = 2\sqrt{2}\left(1 - \sqrt{h_c^*}\right) \quad (34)$$

209 Applying Eq. (34) in Eq. (32) yields the dimensionless location and celerity of the junction

210  $N-N$ :

$$211 \quad X_N = C_2^* T \quad (35)$$

$$212 \quad C_2^* = \sqrt{2}\left(2 - 2.5\sqrt{h_c^*}\right) \quad (36)$$

213 The dimensionless discharge and the Froude Number are expressed as:

$$214 \quad Q_c^* = 2\sqrt{2}\left(h_c^*\right)^2\left(1 - \sqrt{h_c^*}\right) \quad (37)$$

$$215 \quad F_{rc} = 2\sqrt{2}\left(\frac{1}{\sqrt{h_c^*}} - 1\right) \quad (3$$

216 8)

217 Applying Eq. (34) in Eq. (13) yields the dimensionless wave-front celerity:

$$218 \quad \xi^* = 2\sqrt{2}\frac{\left(h_c^*\right)^2\left(1 - \sqrt{h_c^*}\right)}{\left(h_c^*\right)^2 - \left(h_d^*\right)^2} \quad (39)$$

219 The dimensionless shock location is expressed as:

$$220 \quad X_R = T\xi^* \quad (40)$$

221 where  $X_R = x_R/h_u$ .

222

## 223 **Experimental Setup and Flow Measurement Technique**

224 The experiments are performed in a triangular flume of 18 m in length, 1 m width and 1.09 m in

225 height with a horizontal bottom, as shown in Fig. 2. One side wall is vertical for recording the flow

226 with cameras and the slope of the other side wall is 45°. The flume is made of stalinite supported by

227 a steel frame and is separated by a 15-mm-thick fiberglass plate into two sections with the upstream  
228 and the downstream length being 8.37 m and 9.63 m, respectively. The instantaneous dam break is  
229 simulated by lifting the plate instantly with an electromagnetic brake asynchronous motor. A new  
230 criterion for the maximum plate removal time in non-rectangular channels proposed by Wang et al.  
231 (2019) is used:

$$232 \quad t_{\max} = \sqrt{2h_0 / g} \quad (41)$$

233 where  $h_0$  = average water depth upstream of the plate, i.e.,  $h_0 = A_u/B_u$ , ( $A_u$  and  $B_u$  = initially upstream  
234 cross-sectional area and water surface width, respectively). Eq. (41) has the same form of the one  
235 suggested by Lauber and Hager (1998a) in which  $h_0$  is defined as the upstream water depth. The  
236 plate removal time is around 0.1024 s, 0.1250 s and 0.1875 s for the upstream water depth of 0.2 m,  
237 0.4 m and 0.6 m, respectively, satisfying the transient failure condition. A steel gate is located at the  
238 downstream end of the channel for providing different wet bed conditions.

239 To obtain the free surface profiles along the channel and the time evolution of water levels,  
240 digital image processing that is based on the camera video of the water flow is used. The digital  
241 imaging system contains three parts: a computer, eight high-speed CCD cameras and the MATLAB  
242 software (MATLAB 2016) in which camera calibration, frame grab, synchronous images  
243 combination and binarization are conducted. The CCD cameras are arranged along the flume and in  
244 parallel at the same side of the flume with equal interval of 1.4 m to capture the evolution of the  
245 water flow. Cameras are turned on wirelessly by a remote control in order to make cameras work  
246 synchronously. Some auxiliary facilities are adopted for ensuring the quality of the video and  
247 conveniently applying the image processing technology, such as covering the slopping wall of  
248 channel with a smooth white car sticker, dyeing the water with methyl violet, and sheltering the  
249 cameras and the channel from the light. The flow measurement includes calibration process and  
250 water depth acquisition. Details about the flow measurement adopted in the present experiment can  
251 be found in Wang et al. (2019, 2020b). The parameters of total 30 runs are listed in Table 1, which

252 includes three different initial impoundment depths and ten dimensionless water depths.

253

## 254 **Results**

### 255 *Discussion of Analytical Solutions*

256 The dimensionless depth, velocity, discharge and the Froude number against the dimensionless  
257 variable  $X/T$  are shown in Fig. 3, in which the analytical solution by Ritter (1892) for rectangular  
258 channels is included for comparison. The value of  $X/T$  in the triangular channels ranges from  
259  $-\sqrt{2}/2$  to  $2\sqrt{2}$ , corresponding to  $h^* = 1$  and  $h^* = 0$  respectively, while it varies from  $-1$  to  $2$  in  
260 rectangular channels. The depth decreases with the increase of  $X/T$ ; and the water depth in the  
261 triangular channels is overall larger than that in the rectangular channels. The value of water depth is  
262  $16/25$  and  $4/9$  at the dam site (i.e.,  $X/T = 0$ ,  $x = 0$ ) for the triangular and rectangular channels,  
263 respectively. The velocity increases with the increase of  $X/T$ . The velocity curves in the two channels  
264 intersect with each other at  $X/T = 5 - 3\sqrt{2}$  with  $u^* = 2(2 - \sqrt{2})$ . The velocity in the rectangular  
265 channels is larger than that in the triangular channels for  $X/T < 5 - 3\sqrt{2}$ ; and the contrary is the case  
266 for  $X/T > 5 - 3\sqrt{2}$ . The discharge increases first and respectively reaches the peak of  $0.232$  and  
267  $0.296$  at the dam site for the triangular and rectangular channels, and then decreases with the increase  
268 of  $X/T$ . The depth, velocity and discharge in both channels remain constant at the dam site as the time  
269 goes by.

270 It is seen that  $F_r$  increases with the increase of  $X/T$ . The Froude number in the triangular and  
271 rectangular channels respectively equals to zero at  $X/T = -\sqrt{2}/2$  and  $-1$  (corresponding to the  
272 location for the leading edge of the rarefaction surge) and respectively equals to one at  
273  $X/T = 2(\sqrt{2} - 1)/(2\sqrt{2} + 1)$  and  $X/T = 0$ . It is indicated that the transition of flow regime from

274 subcritical to supercritical in triangular channels takes place downstream of the dam, while it occurs  
 275 just at the dam site in rectangular channels.  $F_r$  approaches infinity at  $X/T = 2\sqrt{2}$  and 2 for the  
 276 triangular and rectangular channel, respectively, corresponding to the front of the leading edge of the  
 277 positive surge. This won't be true in practice due to the effect of friction.

278 Fig. 4 presents the profiles of  $h_c^*$ ,  $h_c^* - h_d^*$ ,  $u_c^*$  and  $Q_c^*$  against  $h_d^*$ , containing the  
 279 analytical solution by Stoker (1957) for rectangular channels. It is shown from both Eq. (30) and the  
 280 Stoker's solution that the water depth in Zone 3 (i.e.,  $h_c$ ) is determined only by  $h_d^*$ . When the  
 281 downstream channel bed is initially dry, i.e.,  $h_d = 0$ , it is well known that there is no bore and the  
 282 water depth in Zone 3 is equal to zero, i.e.,  $h_c = 0$ . Fig. 4 shows that  $h_c^*$  increases with the increase  
 283 of  $h_d^*$  and reaches the maximum value of 1 (i.e.,  $h_c^* = 1$ ) when the initial water depth downstream  
 284 is equal to that upstream of a dam, i.e.,  $h_d^* = 1$ .  $h_c^*$  in the triangular channels is smaller than that in  
 285 the rectangular channels; and the difference becomes smaller with increasing  $h_d^*$ .

286 If  $h_d$  is larger than zero (i.e. the initial downstream bed is wet), a bore will be formed. The bore  
 287 height, i.e., the quantity of  $h_c - h_d$ , is a feature of interest under investigation. When  $h_d = 0$ , there is no  
 288 bore and the value of  $h_c - h_d$  is equal to zero. The bore height must again approach zero when  $h_d = h_u$ ,  
 289 i.e., the reservoir head is the same as the tailwater depth. It is seen from Fig. 4 that the dimensionless  
 290 bore height increases sharply with the increase of  $h_d^*$  and respectively reaches the maximum of  
 291 0.286 and 0.309 at  $h_d^* = 0.230$  and 0.176 in the triangular and rectangular channels; and then  
 292 gradually decreases to zero at  $h_d^* = 1$  (i.e.,  $h_d = h_u$ ).

293 As shown in Fig. 4, the dimensionless velocity in Zone 3, which presents an inverse relation of  
 294 the dimensionless tailwater depth, decreases sharply for the range of  $0 < h_d^* < 0.1$  and then gradually  
 295 decreases to zero when  $h_d^* = 1$ .  $u_c^*$  with a maximum of  $2\sqrt{2}$  at  $h_d^* = 0$  in the triangular channels

296 is larger than that with a maximum of 2 in the rectangular channels.

297 When  $h_d^* = 0$ , there is no bore and the discharge  $Q_c^*$  in Zone 3 must be zero. On the other  
298 hand, when  $h_c^*$  approaches the other extreme value, i.e.,  $h_c^* = 1$ , it is indicated from Eq. (37) that  
299  $Q_c$  is again equal to zero. Fig. 4 shows that  $h_c^* = 1$  when  $h_d^* = 1$ . Therefore,  $Q_c$  must reach a  
300 maximum for a certain value of  $h_d^*$ . It is seen that  $Q_c^*$  increases sharply with the increase of  $h_d^*$   
301 and respectively reaches the maximum of 0.232 and 0.296 at  $h_d^* = 0.377$  and 0.138 in the triangular  
302 and rectangular channels (corresponding to  $h_c^* = 16/25$  and  $4/9$ , respectively) and then decreases to  
303 zero when  $h_d^* = 1$  (corresponding to  $h_c^* = 1$ ).

304 Table 2 compares the analytical values for special parameters of dam-break flow to visually  
305 identify the differences between the hydraulic properties for the triangular and the rectangular  
306 channels, including the wave celerities, i.e.,  $C_1^*$ ,  $C_2^*$  and  $\xi^*$ , which will be further discussed  
307 through the comparison with experimental results in the Section “Location and Celerity of  
308 Dam-break Wave Front”.

### 309 ***Dam-break Wave Evolution***

310 Fig. 5 presents the video images of flow evolution for four tailwater depths with  $h_u = 0.4$  m. On each  
311 frame shown in Fig. 5 from top to bottom, the images represent the flow patterns with  $h_d^* = 0.2, 0.4,$   
312  $0.6$  and  $0.8$ , respectively. The water surface in the reservoir declines when the rarefaction wave front  
313 arrives after the dam breaks. It can be seen that the fall of water surface is larger for smaller value of  
314  $h_d^*$ . When the tailwater depth is not large (i.e.,  $h_d^* \leq 0.4$ ), the water surface profile is characterized  
315 by a drop-down curve. For large tailwater depth (i.e.,  $h_d^* \geq 0.5$ ), extra negative waves are formed in  
316 the reservoir which are originated from the dam site and propagate towards the upstream end due to  
317 the tailwater induced resistance force, leading to the undulation of water surface. Comparing with the

318 experiments of Wang et al. (2019), the inception value of  $h_d^*$  for the formation of extra negative  
319 waves is smaller in the rectangular channels than that in the triangular channels, i.e., extra negative  
320 waves are formed for  $h_d^* \geq 0.4$  in the rectangular channels.

321 Once the gate is removed, the tailwater is pushed by the initial reservoir water flow due to the  
322 gravity effect; and the tailwater resists to the drag force. The position of the dam-break wave front  
323 falls behind for a given time as the dimensionless tailwater depth  $h_d^*$  increases. When the value of  
324  $h_d^*$  is very small, the effect of the downstream initial water on the propagation of the dam-break  
325 wave is insignificant. For middle value of  $h_d^*$  (e.g.,  $h_d^* = 0.2-0.4$ ), a significant interaction  
326 between the initial reservoir water and the tailwater is observed. The dam-break wave front is broken,  
327 and a jet is formed downstream during the initial stage, which forces the flow to move upward, as  
328 seen in the upper two frames in Fig. 5. The jet falls back down the tailwater and produces air  
329 entrainment, causing substantial foaming in the free surface of the wave front. This jet-like  
330 phenomenon is also observed in the study of Wang et al. (2019), which is quite similar to the  
331 behavior of the dam-break flow at the initial stages in the rectangular channels (Stansby et al. 1998;  
332 Ozmen-Cagatay and Kocaman 2010; and Kocaman and Ozmen-Cagatay 2015). When  $h_d^*$  is large  
333 (e.g.,  $h_d^* = 0.6$  and  $0.8$ ), the jet and the resultant air entrainment are not observed, instead the  
334 undular bores are formed, which are similar to the Favre Waves (Favre 1935; Benet and Cunge 1971;  
335 Treske 1994; Prüser and Zielke 1994; Soares-Frazão and Zech 2002). The wavelength of the waves  
336 increases with the increase of the downstream initial water depth. Accordingly, the frequency of the  
337 waves (i.e., the number of waves passing a given cross-section per unit time) decreases as the  
338 propagation speed decreases. The time evolutions of dam-break flow with  $h_u = 0.6$  m are similar to  
339 those with  $h_u = 0.4$  m.

340

341 ***Water Surface Profiles***

342 Fig. 6 shows the comparison of the measured analytically solved water surface profiles along the  
343 channel at  $t = 0.5$  s, 1.0 s, 1.5 s, 2.0 s, 2.5 s, 3.0 s and 3.5 s for different  $h_d^*$ . For the sake of  
344 clarification, only the water surface profiles in the range of  $h^*$  between 0.5 and 1.0 are presented  
345 when  $h_d^* \geq 0.5$ . For  $h_d^* \leq 0.4$ , both the analytical and experimental results show that the  
346 dimensionless water surface profiles in the reservoir at a specific time overlap each other for  
347 different tailwater depths; and the effect of  $h_d^*$  on the propagation of the rarefaction wave front is  
348 insignificant. This may be explained using the analytical model as following. When  $h_d^* \leq 0.377$ , the  
349 junction of Zone 2 and Zone 3 is located at the downstream side of the dam, the shock wave has no  
350 influence on the flow upstream of the junction. The prediction of water surface upstream of dam by  
351 analytical model reasonably agrees with the measurements except for the rarefaction wave front. It  
352 can be seen from the enlarged views that the rarefaction wave front in the experiments moves  
353 faster than that predicted by the analytical model. The analytical model shows that the dimensionless  
354 water depth at the dam section for  $h_d^* \leq 0.377$  is 16/25, which agrees well with the measurements of  
355 0.6–0.7.

356 Fig. 6 shows the strong dependence of the dam-break flow movement in the reach downstream  
357 of the dam on  $h_d^*$ . The shock wave front propagates slower when  $h_d^*$  is larger. The displacement  
358 difference of the shock wave fronts for different values of  $h_d^*$  becomes larger with the lapse of time.  
359 It is found that the analytical model can well predict the water surface profile after the water rise  
360 formed downstream of the dam disappears which cannot be provided by the analytical solution. The  
361 wave front predicted by the analytical model is located in front of the measured one, partly due to the  
362 omission of bed friction in the analytical model. Such difference between prediction and  
363 measurement becomes smaller with the decrease of  $h_d^*$ .

364 Fig. 6 (b) shows that both the measured water surfaces upstream and downstream of the dam

365 fluctuate around the analytically predicted water surface profiles for  $h_d^* \geq 0.5$ . It is seen that the  
366 measured rarefaction wave front travels faster than that predicted by the analytical model. The  
367 position of the shock wave front predicted by the analytical model has better agreement with the  
368 measurement for  $h_d^* \geq 0.5$  than that for  $h_d^* \leq 0.4$ . The measured and analytically predicted water  
369 surface profiles at  $t = 0.5\text{--}3.5$  s for different values of  $h_d^*$  with  $h_u = 0.6$  m are similar to those with  
370  $h_u = 0.4$  m.

371

### 372 *Time Evolution of Water Level*

373 The stage hydrographs at seven locations (i.e.,  $x = -7, -4, -2, -0.16, 2, 4$  and  $6$  m) are acquired  
374 directly from the synchronous recorded images. Fig. 7 shows the comparison of the measured and  
375 predicted temporal evolution of water depth at all chosen positions with  $h_u = 0.4$  m. In the reservoir,  
376 the rarefaction wave leads to a decline of water level at all locations. When  $h_d^* \leq 0.4$ , the stage  
377 hydrographs for different values of  $h_d^*$  at a chosen position are close to each other, which is well  
378 captured by analytical model. It is seen that the inception of water level fall predicted by the  
379 analytical model is later than that measured, and the lag becomes small towards the dam site. It is  
380 shown that the rarefaction wave front provided by the analytical model propagates slower than the  
381 measured one. Analytical solution shows that the predicted stage hydrographs collapse in the  
382 reservoir region. At the farthest upstream section ( $x = -7$  m), the stage hydrographs predicted by the  
383 analytical model deviate from the measurements. The reason is that when the rarefaction wave  
384 arrives at the upstream end of channel, sufficient water volume cannot be provided due to the limited  
385 reservoir length, resulting in a quick drop of water surface. The inception of deviation takes place  
386 earlier at the section that is closer to the upstream end of channel.

387 The water level downstream of the dam rises quickly as the shock wave arrives and reaches to

388 a stable state finally. The inception of water level rise is later for larger value of  $h_d^*$ , indicating that  
389 the shock wave front travels slower with the increase of  $h_d^*$ . Both the change of water level over the  
390 time and the stable depth are predicted very well by the analytical model, except that the predicted  
391 water level has very sharper increase than the measurement at early stage.

392 When  $h_d^* \geq 0.5$ , extra negative waves occur in the reservoir, causing the water level  
393 undulating over time. The undulation begins earlier for large value of  $h_d^*$ . In addition, the undulation  
394 amplitude becomes larger towards the dam. The analytical solution shows that the undulation  
395 attenuates with the time for a given location and the water level tends to be stable. The undulation of  
396 water level is also found in the reach downstream of the dam. For a given location, the inception of  
397 undulation takes place later when the value of  $h_d^*$  is larger, because the shock wave front propagates  
398 slower. Similar to the situation in the reservoir, the attenuation of the undulation with the time is  
399 found for a given location and the predicted water level agrees well with the measurements,  
400 indicating that the analytical model is able to predict the stable water level in the reaches both the  
401 upstream and downstream of the dam.

402 The measured and analytically predicted temporal evolutions of water depth at all chosen  
403 positions with  $h_u = 0.6$  m are similar to those with  $h_u = 0.4$  m.

404

#### 405 ***Location and Celerity of Dam-break Wave Front***

406 Fig. 8 shows the comparison between the measured and analytically predicted locations of shock  
407 wave fronts  $X_R$  with the time  $T$  under different values of  $h_d^*$  for three reservoir heads. The time  
408 interval of experimental results is 0.5 s. It is shown that the analytical prediction satisfactorily agrees  
409 with the measurement for  $h_d^* \geq 0.3$ , indicating that the shock wave front propagates with an  
410 approximately constant speed along the flume. When  $h_d^* \leq 0.1$ , the variation of  $X_R$  with  $T$  may be

411 characterized by a parabolic curve, showing that the wave-front celerity decreases along the flume. A  
 412 linear relationship is also found between the shock wave-front locations  $X_R$  and the time  $T$ , as shown  
 413 in Fig. 8. The wave front moves slower with the increase of the tailwater depth. It is seen that the  
 414 analytically predicted shock wave front for  $h_d^* = 0.0$  moves much faster than the measured shock  
 415 wave front does. This large difference could be ascribed to the fact that the analytical model ignores  
 416 bed friction, which plays an important role for small  $h_d^*$ . Fig. 8 also shows that the effect of  $h_d^*$  on  
 417 the shock wave front weakens with the increase of  $h_d^*$ .

418 Fig. 9 shows the comparison of the predicted and measured locations of the rarefaction wave  
 419 tail (i.e.,  $X_N$ ) with the time  $T$  for different  $h_d^*$  and three reservoir heads. It is seen that the analytical  
 420 model can provide good results when  $h_d^* \geq 0.3$ . It is obtained from Eq. (36) that when  $h_c^* = 16/25$ ,  
 421 corresponding to  $h_d^* = 0.377$ , the rarefaction wave tail is located at the dam site (i.e.,  $X_N = 0$ ),  
 422 indicating that the rarefaction wave tail is observed in the downstream reach of the dam for  $h_d^* <$   
 423  $0.377$  and occurs in the reservoir for  $h_d^* > 0.377$ . The analytical model is well validated with the  
 424 measurements. For the rectangular channel, the location of the rarefaction wave tail at the dam site  
 425 requires a smaller tailwater depth, i.e.,  $h_d^* = 0.138$ , corresponding to  $h_c^* = 4/9$ .

426 Fig. 10 shows the comparison between the measured and analytically predicted locations of  
 427 rarefaction wave fronts  $X_M$  with the time  $T$  for different  $h_d^*$  and three reservoir heads. The analytical  
 428 model provides rarefaction wave front propagation with a constant speed, which is independent of  
 429 the tailwater level. Fig. 10 shows that the analytical model slightly underestimates the location of  
 430 rarefaction wave front when  $h_d^* < 0.4$  and provides good prediction for  $h_d^* \geq 0.4$ .

431 Fig. 11 presents the dimensionless celerity of rarefaction wave front, rarefaction wave tail and  
 432 shock wave front against the dimensionless tailwater depth  $h_d^*$ , in which the analytical solution by

433 Stoker (1957) for the rectangular channel is included for comparison. For a given  $h_d^*$ , the  
 434 experimental celerities will be approximated by the steady values which are equal to the celerities at  
 435  $x = -7.5$  m and  $7.5$  m for the rarefaction wave front and the shock wave front, respectively. The  
 436 dimensionless distances from the dam site are  $X = \pm 37.5, \pm 18.75, \pm 12.5$  for  $h_u = 0.2$  m,  $0.4$  m,  $0.6$  m,  
 437 respectively. It is seen that the predicted rarefaction wave front propagates with a constant speed of  
 438  $C_1^* = -\sqrt{2}/2$ , which is slightly slower than the measured celerity of the rarefaction wave front when  
 439  $h_d^* < 0.4$ , while the predicted  $C_1^*$  agrees well with the measurements for  $h_d^* \geq 0.4$ . It is also shown  
 440 that the tailwater depth has insignificant effects on the movement of the rarefaction wave front. The  
 441 curve of  $C_1^* = -1$  for the rectangular channel is under the one in the triangular channel, indicating  
 442 that the rarefaction wave front travels faster in the former channel.

443 Both the analytical prediction and measurement show that  $C_2^*$  decreases rapidly as  $h_d^*$   
 444 ranges from 0 to 0.2, and then gradually decreases with the increase of  $h_d^*$ . It is seen that the  
 445 analytical model accurately predicts the propagation speed of the rarefaction wave tail (i.e.,  $C_2^*$ )  
 446 when  $h_d^* \geq 0.3$  and slightly over-predicts the speed for  $h_d^* < 0.2$ . When  $h_d^* = 0$ , the measured  $C_2^*$   
 447 (approximate 1.6) has the identical value as the shock wave front celerity  $\xi^*$ , and is smaller than the  
 448 analytical prediction of  $2\sqrt{2}$ . It can be seen that the analytical prediction for the shock wave front  
 449 celerity agrees well with the measurement when the value of  $h_d^*$  is larger than 0.2. The curve for the  
 450 analytical solution of  $C_2^*$  in the rectangular channel drops from 2 to  $-1$  throughout the entire range  
 451 of  $h_d^*$ , intersecting with the  $x$  axis at  $h_d^* = 0.138$  for which the rarefaction wave tail is located in the  
 452 dam site. The shock wave front celerity  $\xi^*$  decreases monotonically from  $2\sqrt{2}$  to  $\sqrt{2}/2$  in the  
 453 entire range of  $h_d^*$  in the triangular channel, while it drops from 2 to the minimum of 0.936 at  
 454  $h_d^* = 0.349$  and then grows slowly to 1 in the rectangular channel. The curves of  $\xi^*$  intersect with

455 each other at  $h_d^* = 0.281$  with  $\xi^* = 0.938$ . The value of  $\xi^*$  in the triangular channel is larger than  
456 that in the rectangular channel for  $h_d^* < 0.281$ , and the contrary is true for  $h_d^* > 0.281$ . The  
457 dimensionless celerities for three different initial reservoir depths are close at the same value of  $h_d^*$   
458 for both  $C_2^*$  and  $\xi^*$ . However, the measured  $C_1^*$  at  $h_u = 0.6$  m slightly deviates from those under  
459  $h_u = 0.2$  m and  $0.4$  m. The reason is that  $C_1^*$  decreases with the distance and tends to reach a steady  
460 value, while the steady state for  $C_1^*$  under  $h_u = 0.6$  m is not reached due to the limited reservoir  
461 length.

462

### 463 **Conclusions**

464 In the present study, an analytical model that is based on the method of characteristics, has been  
465 developed for the instantaneous dam-break floods down a horizontal and frictionless channel with a  
466 triangular cross-section. The variation of the dimensionless water depth  $h^*$ , velocity  $u^*$  and discharge  
467  $Q^*$ , and the Froude number with the dimensionless variable  $X/T$  has been discussed. The variation of  
468 dimensionless depth  $h_c^*$ , bore height  $h_c^* - h_d^*$ , velocity  $u_c^*$ , discharge  $Q_c^*$ , and the Froude number  
469 in Zone 3, and wave-front celerities (i.e.,  $C_1^*$ ,  $C_2^*$ ,  $\xi^*$ ) against  $h_d^*$  is investigated. Laboratory  
470 experiments of dam-break flows have been conducted in a prismatic, horizontal, triangular and  
471 smooth flume, covering a wide range of initial reservoir heads and tailwater levels. Digital image  
472 processing, which is a non-intrusive flow measurement technique, is adopted in the experiments to  
473 provide the temporal evolution of the free surface profiles along the whole channel. The analytical  
474 model is well validated using the laboratory measurements. The comparisons between the analytical  
475 results and the well-known solutions by Ritter (1892) and Stoker (1957) for rectangular channels are  
476 also presented. The following conclusions can be drawn:

477 (1) When the tailwater depth is not large (i.e.,  $h_d^* \leq 0.4$ ), the dimensionless water surface  
478 profiles in the reservoir for different  $h_d^*$  are characterized by drop-down curves, which overlap each  
479 other at some specific time. The tailwater depth has insignificant influence on the rarefaction wave  
480 propagation. The analytical model shows satisfactory agreement with the measured water surface  
481 profile upstream of the dam, though the predicted rarefaction wave front is slightly slower than the  
482 measured one. The analytical solution for the dimensionless water depth at the dam section is 16/25,  
483 which is within the range of around 0.6–0.7 measured in the tests. It is found that the dependence of  
484 the movement of dam-break flows downstream of the dam on the tailwater depth is strong. The  
485 shock wave front propagates slower for larger value of  $h_d^*$  and the displacement difference of shock  
486 wave fronts for different  $h_d^*$  becomes larger with time.

487 (2) When the tailwater depth is sufficiently large (i.e.,  $h_d^* \geq 0.5$ ), there are extra negative  
488 waves generated in the reservoir, leading to the undulations of water surface whose profile is related  
489 to the value of  $h_d^*$ . In the downstream reach, a rise of water surface is found close to the dam and  
490 becomes weaker for larger value of  $h_d^*$ . Such water rise will evolve into undulations in the end. The  
491 analytical model can provide a stable value for the undulations and is not able to predict the varying  
492 undulations. For the same value of  $h_d^*$ , the dam-break flow evolutions and the water surface profiles  
493 under different reservoir heads remain similar. The significant discrepancy is that the fronts of  
494 dam-break waves (i.e., rarefaction waves, extra negative waves and shock waves) propagate faster  
495 for a larger reservoir head, resulting in an earlier inception for the changes of water surfaces both in  
496 the reservoir and the downstream reach.

497 (3) The profiles of  $h^*$ ,  $u^*$ ,  $Q^*$  and  $Fr$  along  $X/T$  as well as the variations of  $h_c^*$ ,  $h_c^* - h_d^*$ ,  $u_c^*$   
498 and  $Q_c^*$  against  $h_d^*$  in the triangular channel are found similar to those in the rectangular channel.

499  $h^*$  decreases monotonically, while  $u^*$  and  $Fr$  increases in the whole range of  $X/T$ .  $Q^*$  increases first to  
500 the peak at the dam site and then declines to zero. The depth, velocity and discharge at the dam site  
501 keep invariant with time.  $h_c^*$  increases from zero to one with increasing  $h_d^*$ , while  $u_c^*$  drops from  
502 the maximum to zero. Both  $h_c^* - h_d^*$  and  $Q_c^*$  increase sharply to the peak and then fall down to  
503 zero at  $h_d^* = 0$ . The rarefaction wave front propagates upstream with a constant speed, while the  
504 celerity of the rarefaction wave tail drops downstream of the dam and increases in the reservoir with  
505  $h_d^*$ .

506 (4) The differences between the hydraulic properties in the two channels are also identified  
507 analytically, which should be related to the discrepancy in the hydraulic ratio of channels. The range  
508 of  $X/T$  is between  $-\sqrt{2}/2$  and  $2\sqrt{2}$  in the triangular channels, while it varies from  $-1$  to  $2$  in the  
509 rectangular channels.  $h^*$  in the triangular channels are overall larger than those in the rectangular  
510 channels and the contrary is true for  $Fr$ . The value of  $u^*$  in the rectangular channels is larger than that  
511 in the triangular channels for  $X/T < 5 - 3\sqrt{2}$ ; and the contrary is the case for  $X/T > 5 - 3\sqrt{2}$ . The  
512 peaks of  $Q^*$  are 0.232 and 0.296 for the triangular and rectangular channels, respectively.

513 (5)  $h_c^*$  in the triangular channels is smaller than that in the rectangular channels, while the  
514 contrary is the case for  $u_c^*$ . The peak of  $h_c^* - h_d^*$  are 0.286 and 0.309 and the maximum of  $Q_c^*$   
515 equals 0.232 and 0.296 in the triangular and rectangular channels, respectively. The rarefaction wave  
516 front with  $C_1^* = -\sqrt{2}/2$  in the triangular channels travels slightly slower than that with  $C_1^* = -1$   
517 for the rectangular channels. The rarefaction wave tail with  $C_2^*$  for the triangular channels moves  
518 faster than that for the rectangular channels in the reach downstream of the dam, and the contrary is  
519 true in the reservoir.  $h_d^*$  respectively equals 0.377 and 0.138 in the triangular and rectangular  
520 channels for  $C_2^* = 0$ , which serves as a criterion for determining if the tailwater affects the

521 hydraulics upstream of the dam.  $\xi^*$  presents a monotonic decrease from  $2\sqrt{2}$  to  $\sqrt{2}/2$  in the  
522 triangular channels, while it shows a sharp drop from 2 to the minimum of 0.936 followed by a slow  
523 growth to 1 in the rectangular channels. The shock wave front in the triangular channels propagates  
524 faster than that in the rectangular channels for  $h_d^* < 0.281$ , and the contrary is true for  $h_d^* > 0.281$ .

525 (6) The analytical model accurately predicts the effect of the initial downstream water depth on  
526 the propagation of flood waves generated by the dam break in the triangular channels. The laboratory  
527 data generated in this study with a wide range of tailwater depth could be useful for researchers to  
528 validate their analytical and numerical models of dam-break flows.

529

### 530 **Data Availability Statement**

531 Some or all data, models, or code generated or used during the study are available from the  
532 corresponding author by request (including analytical and experimental test data).

### 533 **Acknowledgements**

534 This study is supported by the National Natural Science Foundation of China (Grant No: 51879179),  
535 Sichuan Science and Technology Program (No. 2019JDTD0007) and Open Fund from the State Key  
536 Laboratory of Hydraulics and Mountain River Engineering, Sichuan University (SKHL1809).

### 537 **Notation**

538 *The following symbols are used in this paper:*

539  $A$  = cross-sectional area;

540  $B$  = water surface width;

541  $C_1$  = rarefaction wave front celerity;

542  $C_2$  = rarefaction wave tail celerity;

543  $F_r$  = Froude Number;

544  $g$  = gravity acceleration;

545  $h$  = flow depth;  
546  $h_0$  = average water depth upstream of the plate,  $h_0 = A_u/B_u$ ;  
547  $\bar{h}$  = centroid water depth;  
548  $Q$  = flow discharge;  
549  $T$  = dimensionless time,  $T = t(g/h_u)^{1/2}$ ;  
550  $t$  = time;  
551  $t_{\max}$  = maximum plate removal time for simulating instantaneous dam break;  
552  $u$  = flow mean velocity;  
553  $X$  = dimensionless distance along flow direction originated from the dam site,  $X = x/h_u$ ;  
554  $x$  = distance along flow direction originated from dam site;  
555  $\eta$  = variable of integration; and  
556  $\zeta$  = shock wave-front celerity.

### 557 **Superscripts**

558 \* = dimensionless quantity.

### 559 **Subscripts**

560  $c$  = reach upstream of the shock;  
561  $d$  = reach downstream of the shock;  
562  $M$  = position of rarefaction wave front;  
563  $N$  = position of rarefaction wave tail;  
564  $R$  = location of shock wave-front; and  
565  $u$  = undisturbed upstream reach.

### 566 **References**

567 Ancy, C., R. M. Iverson, M. Rentschler, and R. P. Denlinger. 2008. "An exact solution for ideal  
568 dam-break floods on steep slopes." *Water Resour. Res.* 44(1): 567–568.  
569 <https://doi.org/10.1029/2007WR006353>

570 Aureli, F., A., Maranzoni, and P., Mignosa. 2014. "A semi-analytical method for predicting the  
571 outflow hydrograph due to dam-break in natural valleys." *Adv. Water Resour.* 63: 38–44.  
572 <http://dx.doi.org/10.1016/j.advwatres.2013.11.001>

573 Bellos, C. V., J. V. Soulis, and J. G. Sakkas. 1992. "Experimental investigation of two-dimensional  
574 dam-break induced flows." *J. Hydraul. Res.* 30 (1): 47–63.  
575 <https://doi.org/10.1080/00221689209498946>

576 Benet, F., and J. A. Cunge. 1971. "Analysis of experiments on secondary undulations caused by  
577 surge waves in trapezoidal channels." *J. Hydraul. Res.* 9(1): 11–33. DOI:  
578 10.1080/00221687109500335

579 Bukreev, V. I., and A. V. Gusev. 2005. "Initial stage of the generation of dam-break waves." *Doklady*  
580 *Phys.* 50 (4): 200–203. <https://link.springer.com/article/10.1134/1.1922561>

581 Chanson, H. 2009. "Application of the method of characteristics to the dam break wave problem." *J.*  
582 *Hydraul. Res.* 47(1): 41–49. <https://doi.org/10.3826/jhr.2009.2865>

583 Chen, H. Y., W. L. Xu, J. Deng, Y. Xue, and J. Li. 2013. "Experimental investigation of pressure load  
584 exerted on a downstream dam by dam-break flow." *J. Hydraul. Eng.* 140 (2): 199–207.  
585 [https://doi.org/10.1061/\(ASCE\)HY.1943-7900.0000743](https://doi.org/10.1061/(ASCE)HY.1943-7900.0000743)

586 Chen, Y. L., C. Wu, and B. Wang. 2011. "Similarity solution of dam-break flow on horizontal  
587 frictionless channel." *J. Hydraul. Res.* 49(3): 384–387.  
588 <https://doi.org/10.1080/00221686.2011.571537>

589 Chow, V. T. 1959. *Open channel hydraulics*. New York: McGraw-Hill.

590 Dressler, R. F. 1952. "Hydraulic resistance effect upon the dam-break functions." *J. Res. Natl. Bur.*  
591 *Stand.* 49(3): 217–225.

592 Dressler, R. F. 1954. "Comparison of theories and experiments for the hydraulic dam-break wave."  
593 *in Proc. Int. Assoc. Scientific Hydrology Assemblée Générale Rome.* 3(38): 319-328.

594 Escoffier, F. F., and M. B. Boyd. 1962. "Stability aspects of flow in open channel." *In: Proceedings*

595 ASCE, vol. 88(NY6): 145–66.

596 Favre, H. 1935. *Etude théorique et expérimentale des ondes de translation dans les canaux*  
597 *découverts*. Dunod, Paris.

598 Fernandez-Feria, R. 2006. “Dam-break flow for arbitrary slopes of the bottom.” *J. Eng. Math.* 54(4):  
599 319–331. DOI:10.1007/s10665-006-9034-5

600 Fraccarollo, L., and E. F. Toro. 1995. “Experimental and numerical assessment of the shallow water  
601 model for two-dimensional dam-break type problems.” *J. Hydraul. Res.* 33 (6): 843–864.  
602 <https://doi.org/10.1080/00221689509498555>

603 Henderson, F. M. 1966. *Open channel flow*. New York: MacMillan.

604 Hogg, A. J. 2006. “Lock-release gravity currents and dam-break flows.” *J. Fluid Mech.* 569: 61–87.  
605 <https://doi.org/10.1017/S0022112006002588>

606 Hunt, B. 1982. “Asymptotic solution for dam-break problems.” *J. Hydraul. Div.* 108(1): 115–126.

607 Hunt, B. 1983. “Asymptotic solution for dam break on sloping channel.” *J. Hydraul. Eng.* 109(12):  
608 1698–1706. [https://doi.org/10.1061/\(ASCE\)0733-9429\(1983\)109:12\(1698\)](https://doi.org/10.1061/(ASCE)0733-9429(1983)109:12(1698))

609 Hunt, B. 1984. “Perturbation solution for dam-break floods.” *J. Hydraul. Eng.* 110(8): 1058–1071.  
610 [https://doi.org/10.1061/\(ASCE\)0733-9429\(1984\)110:8\(1058\)](https://doi.org/10.1061/(ASCE)0733-9429(1984)110:8(1058))

611 Katopodes, N. D., and D. R. Schamber. 1983. “Applicability of dam-break flood wave models.” *J.*  
612 *Hydraul. Eng.* 109(5): 702–721. [https://doi.org/10.1061/\(ASCE\)0733-9429\(1983\)109:5\(702\)](https://doi.org/10.1061/(ASCE)0733-9429(1983)109:5(702))

613 Katopodes, N. D., and T. Strelkoff. 1978. “Computing two-dimensional dam-break flood waves.” *J.*  
614 *Hydraul. Div.* 104(9): 1269–1288.

615 Kocaman, S., and H. Ozmen-Cagatay. 2015. “Investigation of dam-break induced shock waves  
616 impact on a vertical wall.” *J. Hydrol.* 525: 1–12. <https://doi.org/10.1016/j.jhydrol.2015.03.040>

617 LaRocque, L., J. Imran, and M. Chaudhry. 2013. “Experimental and numerical investigations of  
618 two-dimensional dam-break flows.” *J. Hydraul. Eng.* 139(6): 569–579.  
619 [https://doi.org/10.1061/\(ASCE\)HY.1943-7900.0000705](https://doi.org/10.1061/(ASCE)HY.1943-7900.0000705)

620 Lauber, G., and W. H. Hager. 1998a. "Experiments to dambreak wave: horizontal channel." *J.*  
621 *Hydraul. Res.* 36(3): 291-307. <https://doi.org/10.1080/00221689809498620>

622 Lauber, G., and W. H. Hager. 1998b. "Experiments to dambreak wave: sloping channel." *J. Hydraul.*  
623 *Res.* 36(5): 761-773. <https://doi.org/10.1080/00221689809498601>

624 Liu, W. J., B. Wang, Y. L. Chen, C. Wu, and X. Liu. 2018. "Assessing the analytical solution of  
625 one-dimensional gravity wave model equations using dam-break experimental measurements."  
626 *Water.* 10(9): 1261. <https://doi.org/10.3390/w10091261>

627 Liu, W. J., B. Wang, J. M. Zhang, Y. L. Chen, C. Wu, X. Liu, and J. J. Song. 2019. "Experimental  
628 study on dam-break flow under different upstream and downstream initial water depth."  
629 *Advanced Engineering Sciences.* 51(2): 1–9 (in Chinese). doi:10.15961/j.jsuese.201800374

630 Mangeney, A., P. Heinrich, and R. Roche. 2000. "Analytical solution for testing debris avalanche  
631 numerical models." *Pure Appl. Geophys.* 157: 1081–1096.

632 Miller, S., and M. H. Chaudhry. 1989. "Dam-break flows in curved channel." *J. Hydraul. Eng.*  
633 115(11): 1465–1478. [https://doi.org/10.1061/\(ASCE\)0733-9429\(1989\)115:11\(1465\)](https://doi.org/10.1061/(ASCE)0733-9429(1989)115:11(1465))

634 Oertel, M., and D. B. Bung. 2012. "Initial stage of two-dimensional dam-break waves: laboratory  
635 versus VOF." *J. Hydraul. Res.* 50(1): 89–97. <https://doi.org/10.1080/00221686.2011.639981>

636 Ozmen-Cagatay, H., and S. Kocaman. 2010. "Dam-break flows during initial stage using SWE and  
637 RANS approaches." *J. Hydraul. Res.* 48 (5): 603–611.  
638 <https://doi.org/10.1080/00221686.2010.507342>

639 Ozmen-Cagatay, H., and S. Kocaman. 2012. "Investigation of dam-break flow over abruptly  
640 contracting channel with trapezoidal-shaped lateral obstacles." *J. Fluids Eng.* 134(8): 081204.  
641 doi:10.1115/1.4007154

642 Ozmen-Cagatay, H., S. Kocaman, and H. Guzel. 2014. "Investigation of dam-break flood waves in a  
643 dry channel with a hump." *J. Hydro-environ. Res.* 8: 304–315.  
644 <https://doi.org/10.1016/j.jher.2014.01.005>

645 Prüser, H. H., and W. Zielke. 1994. "Undular bores (Favre Waves) in open channels theory and  
646 numerical Simulation." *J. Hydraul. Res.* 32(3): 337–354.  
647 <http://dx.doi.org/10.1080/00221689409498737>

648 Ritter, A. 1892. "Die Fortpflanzung der Wasserwellen." *Z. Ver. Dtsch. Ing.* 36(33): 947–954 (in  
649 German).

650 Sakkas, J. G., and T. Strelkoff. 1973. "Dam-break flood in a prismatic dry channel." *J. Hydraul. Div.*  
651 99(12): 2195–2216.

652 Sakkas, J. G., and T. Strelkoff. 1976. "Dimensionless solution of dam-break flood waves." *J.*  
653 *Hydraul. Div.* 102(2): 171–184.

654 Schamber, D. R., and N. D. Katopodes. 1984. "One-dimensional models for partially breached dams."  
655 *J. Hydraul. Eng.* 110(8): 1086–1102.  
656 [https://doi.org/10.1061/\(ASCE\)0733-9429\(1984\)110:8\(1086\)](https://doi.org/10.1061/(ASCE)0733-9429(1984)110:8(1086))

657 Soares-Frazão, S. S., and Y. Zech. 2002. "Undular bores and secondary waves—Experiments and  
658 hybrid finite-volume modeling." *J. Hydraul. Res.* 40(1): 33–43.  
659 <https://doi.org/10.1080/00221680209499871>

660 Soares-Frazão, S. S., and Y. Zech. 2007. "Experimental study of dam-break flow against an isolated  
661 obstacle." *J. Hydraul. Res.* 45: 27–36 (Extra issue).  
662 <https://doi.org/10.1080/00221686.2007.9521830>

663 Stansby, P., A. Chegin, and T. Barnes. 1998. "The initial stages of dam-break flow." *J. Fluid Mech.*  
664 374: 407–424. doi:10.1017/S0022112098009975

665 Stoker, J. J. 1957. *Water waves: The mathematical theory with applications*. Interscience, New York.

666 Su, S. T., and A. H. Barnes. 1970. "Geometric and frictional effects on sudden release." *ASCE J.*  
667 *Hydraul. Div.* 96(11): 2185–2200.

668 MATLAB. 2016. *Camera calibrator help*. The MathWorks, Inc.

669 Treske, A. 1994. "Undular bores (favre-waves) in open channels - Experimental studies." *J. Hydraul.*

670 *Res*, 32(3): 355–370.

671 Wang, B., Y. L. Chen, C. Wu, Y. Peng, X. Ma, and J. J. Song. 2017. “Analytical solution of  
672 dam-break flood wave propagation in a dry sloped channel with an irregular-shaped  
673 cross-section.” *J. Hydro-environ. Res.* 14: 93–104. <http://dx.doi.org/10.1016/j.jher.2016.11.003>

674 Wang, B., J. M. Zhang, Y. L. Chen, Y. Peng, X. Liu, and W. J. Liu. 2019. “Comparison of measured  
675 dam-break flood waves in triangular and rectangular channels.” *J. Hydrol.* 575: 690–703.  
676 <https://doi.org/10.1016/j.jhydrol.2019.05.081>.

677 Wang, B., Y. L. Chen, Y. Peng, J. M. Zhang, and Y. K. Guo. 2020a. “Analytical solution of shallow  
678 water equations for ideal dam-break flood along a wet bed slope.” *J. Hydraul. Eng.* 146(2):  
679 06019020. [https://doi.org/10.1061/\(ASCE\)HY.1943-7900.0001683](https://doi.org/10.1061/(ASCE)HY.1943-7900.0001683).

680 Wang, B., W. J. Liu, W. Wang, J. M. Zhang, Y. L. Chen, Y. Peng, X. Liu, and S. Yang. 2020b.  
681 “Experimental and numerical investigations of similarity for dam-break flows on wet bed.” *J.*  
682 *Hydrol.* 583: 124598. <https://doi.org/10.1016/j.jhydrol.2020.124598>.

683 Whitham, G. B. 1955. “The effects of hydraulic resistance in the dam-break problem.” *Proc. R. Soc.*  
684 *London.* 227(1170): 399–407.

685 Wu, C., G. Q. Dai, and C. G. Wu. 1993. “Model of dam-break floods for channels of arbitrary cross  
686 section.” *J. Hydraul. Div.* 119(8): 911–923.  
687 [https://doi.org/10.1061/\(ASCE\)0733-9429\(1993\)119:8\(911\)](https://doi.org/10.1061/(ASCE)0733-9429(1993)119:8(911))

688 Wu, C., G. F. Huang, and Y. H. Zheng. 1999. “Theoretical solution of dam-break shock wave.” *J.*  
689 *Hydraul. Eng.* 125(11): 1210–1215.  
690 [https://doi.org/10.1061/\(ASCE\)0733-9429\(1999\)125:11\(1210\)](https://doi.org/10.1061/(ASCE)0733-9429(1999)125:11(1210))

691 Zanuttigh, B., and A. Lamberti. 2011. “Dam-break waves in power-law channel section.” *J. Hydraul.*  
692 *Eng.* 127(4): 322–326. [https://doi.org/10.1061/\(ASCE\)0733-9429\(2001\)127:4\(322\)](https://doi.org/10.1061/(ASCE)0733-9429(2001)127:4(322))

693

694

695 **Figure captions list**

696 Fig. 1. Definition sketch for dam-break waves.

697 Fig. 2. Experimental set up.

698 Fig. 3. Profiles of dimensionless depth, velocity, discharge and Froude number against  $X/T$ .

699 Fig. 4. Profiles of  $h_c^*$ ,  $h_c^* - h_d^*$ ,  $u_c^*$  and  $Q_c^*$  against  $h_d^*$ .

700 Fig. 5. Experimental images of the flow for  $h_d^* = 0.2, 0.4, 0.6$  and  $0.8$  with  $h_u = 0.4$  m (a) in the  
701 reservoir; (b) in the downstream flume.

702 Fig. 6. Comparison of the measured and predicted dimensionless water depth with  $h_u = 0.4$  m for (a)  
703  $h_d^* = 0.1, 0.2, 0.3$  and  $0.4$ ; (b)  $h_d^* = 0.5, 0.6, 0.7, 0.8$  and  $0.9$ .

704 Fig. 7. Comparison of the measured and analytically predicted stage hydrographs at different  
705 positions with  $h_u = 0.4$  m for (a)  $h_d^* = 0.1, 0.2, 0.3$  and  $0.4$ ; (b)  $h_d^* = 0.5, 0.6, 0.7, 0.8$  and  $0.9$ .

706 Fig. 8. Comparison of the measured and predicted locations of shock wave fronts.

707 Fig. 9. Comparison of the measured and predicted locations of rarefaction wave tails.

708 Fig. 10. Comparison of the measured and predicted locations of rarefaction wave fronts.

709 Fig. 11. Comparison of the measured and predicted  $C_1^*$ ,  $C_2^*$  and  $\xi^*$ .

710

711 **Table captions list**

712 Table 1. Test conditions.

713 Table 2. Special parameter values of dam-break flow for triangular and rectangular channels.

714

715

716

717



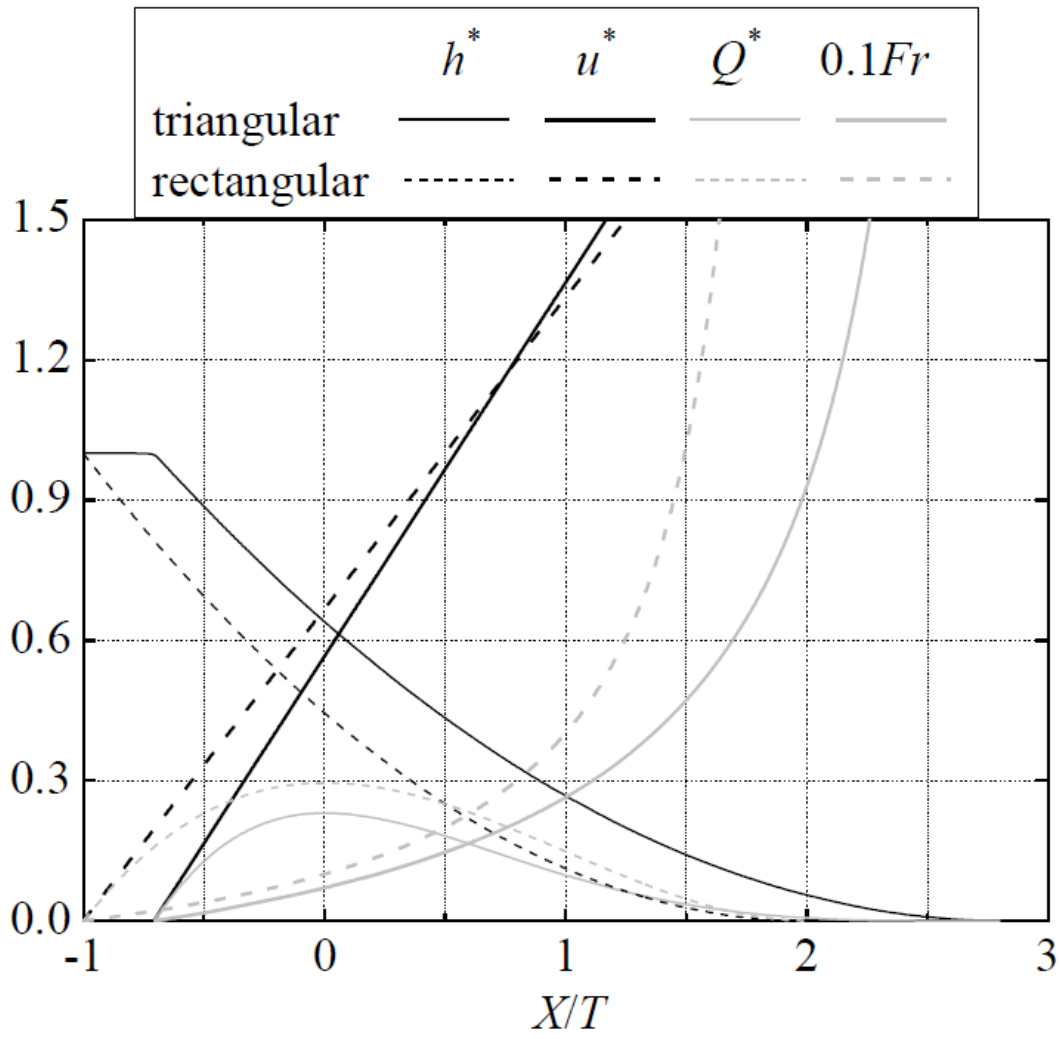


Fig. 3. Profiles of dimensionless depth, velocity, discharge and Froude number against  $X/T$

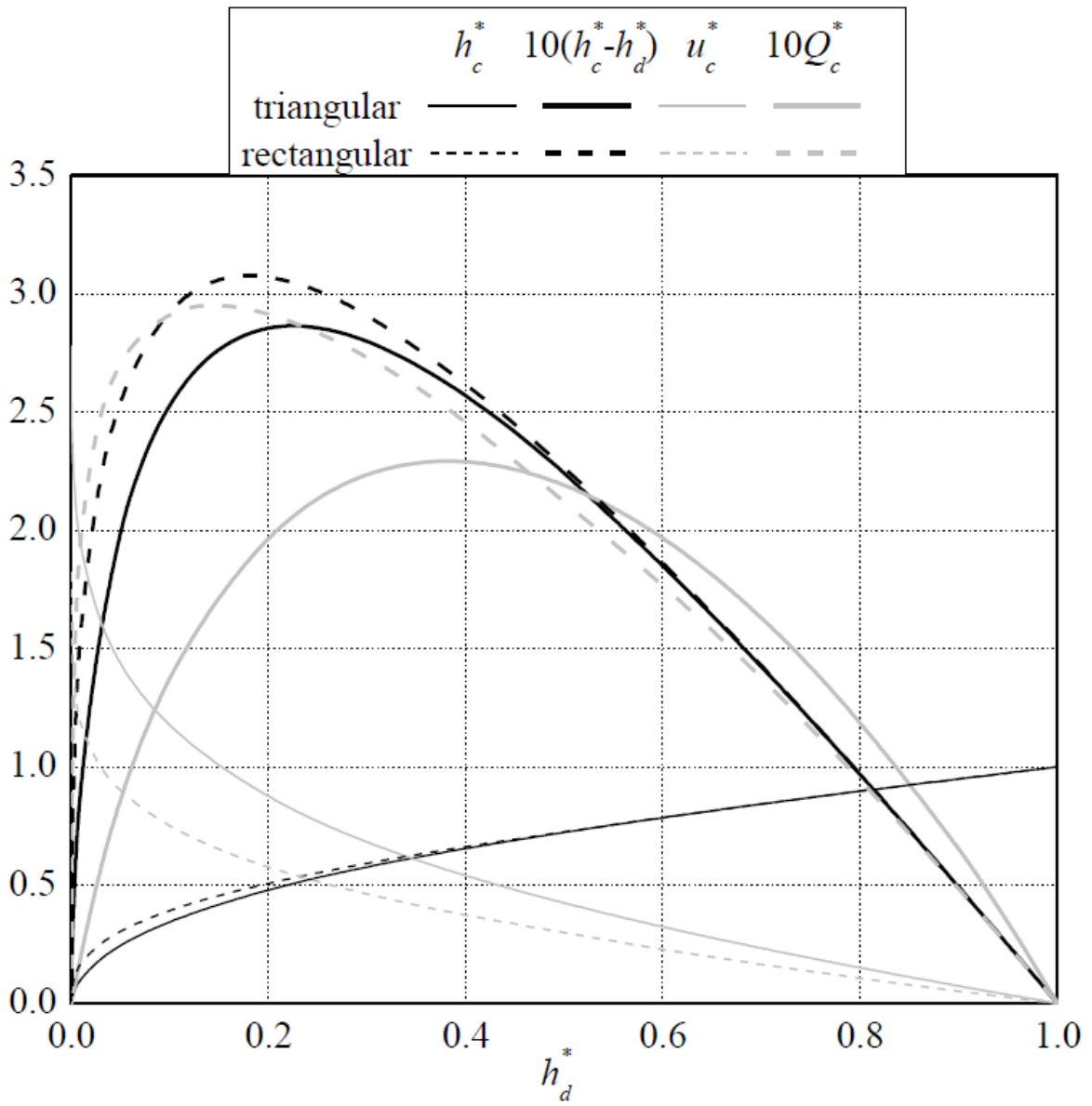
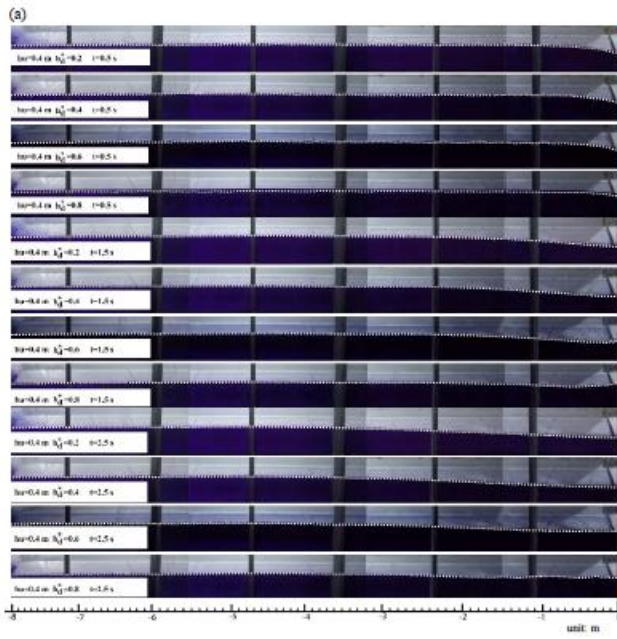


Fig. 4. Profiles of  $h_c^*$ ,  $h_c^* - h_d^*$ ,  $u_c^*$  and  $Q_c^*$  against  $h_d^*$ .



723

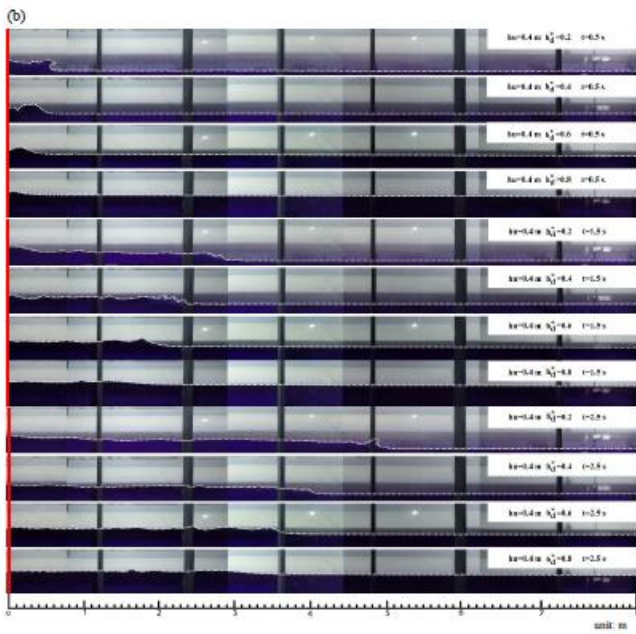
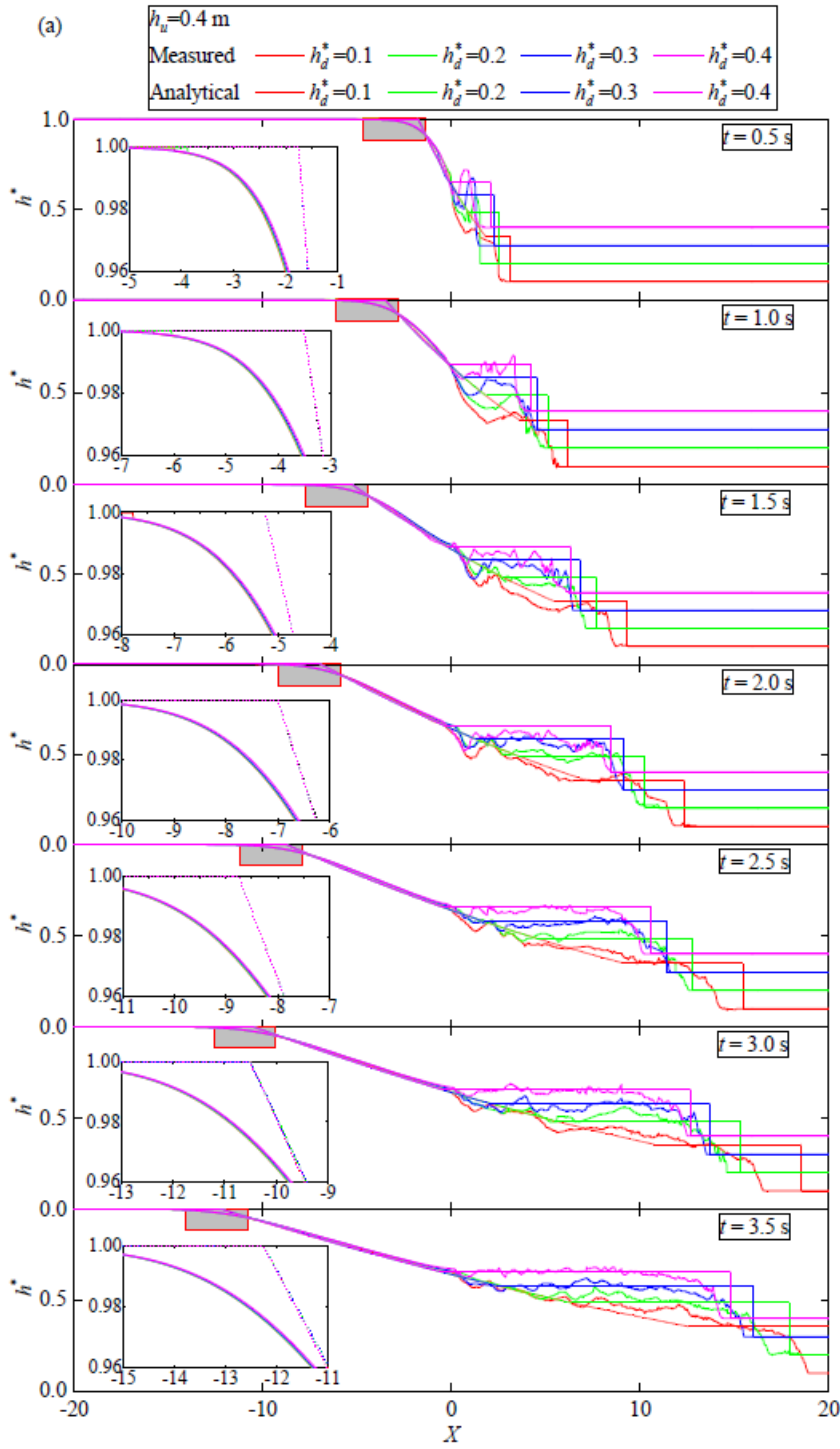


Fig. 5. Experimental images of the flow for  $h_d^* = 0.2, 0.4, 0.6$  and  $0.8$  with  $h_u = 0.4$  m (a) in the reservoir; (b) in the downstream flume. The dam site is indicated with red lines.

724



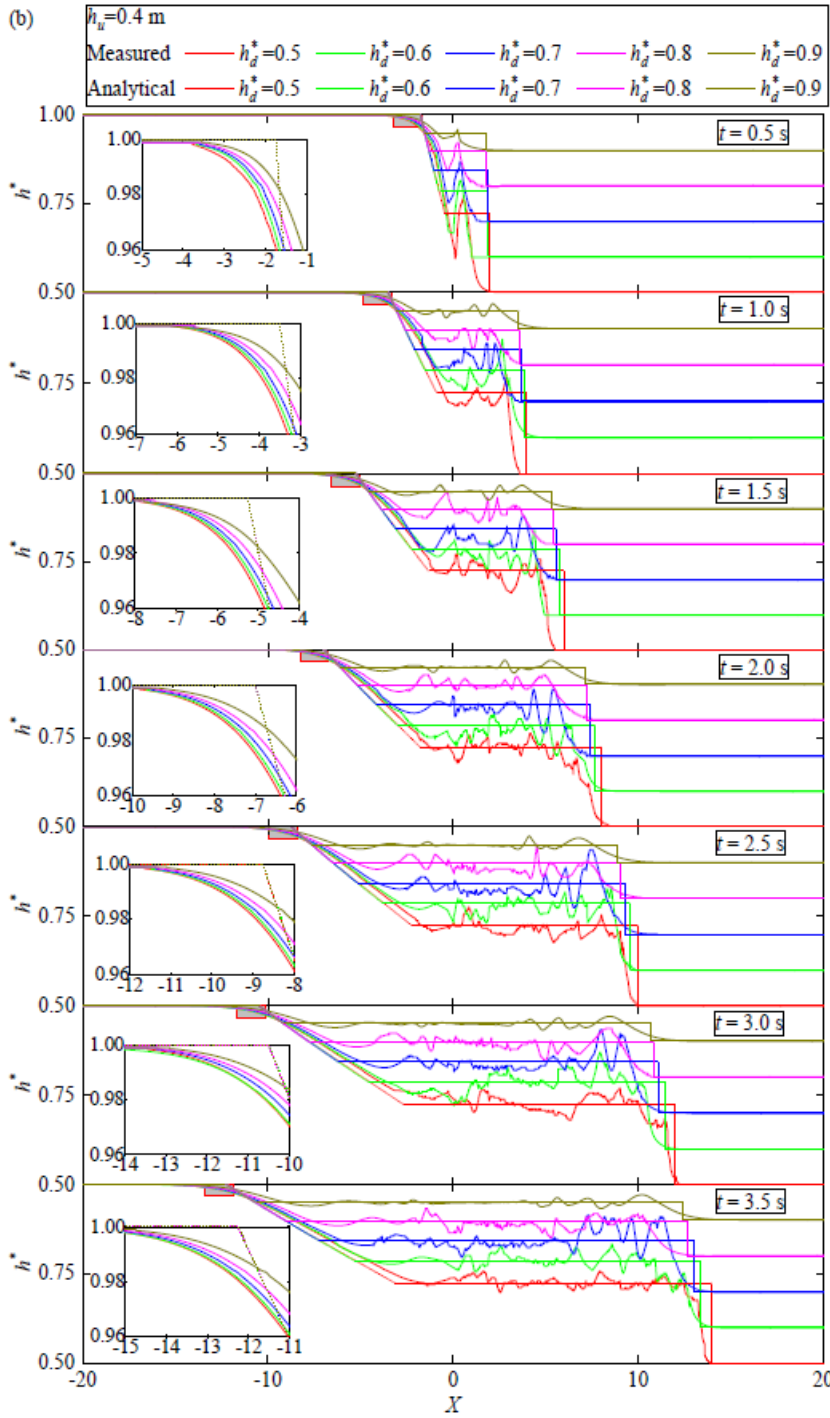


Fig. 6. Comparison of the measured and predicted dimensionless water depth with  $h_u = 0.4$  m for

(a)  $h_d^* = 0.1, 0.2, 0.3$  and  $0.4$ ; (b)  $h_d^* = 0.5, 0.6, 0.7, 0.8$  and  $0.9$ .

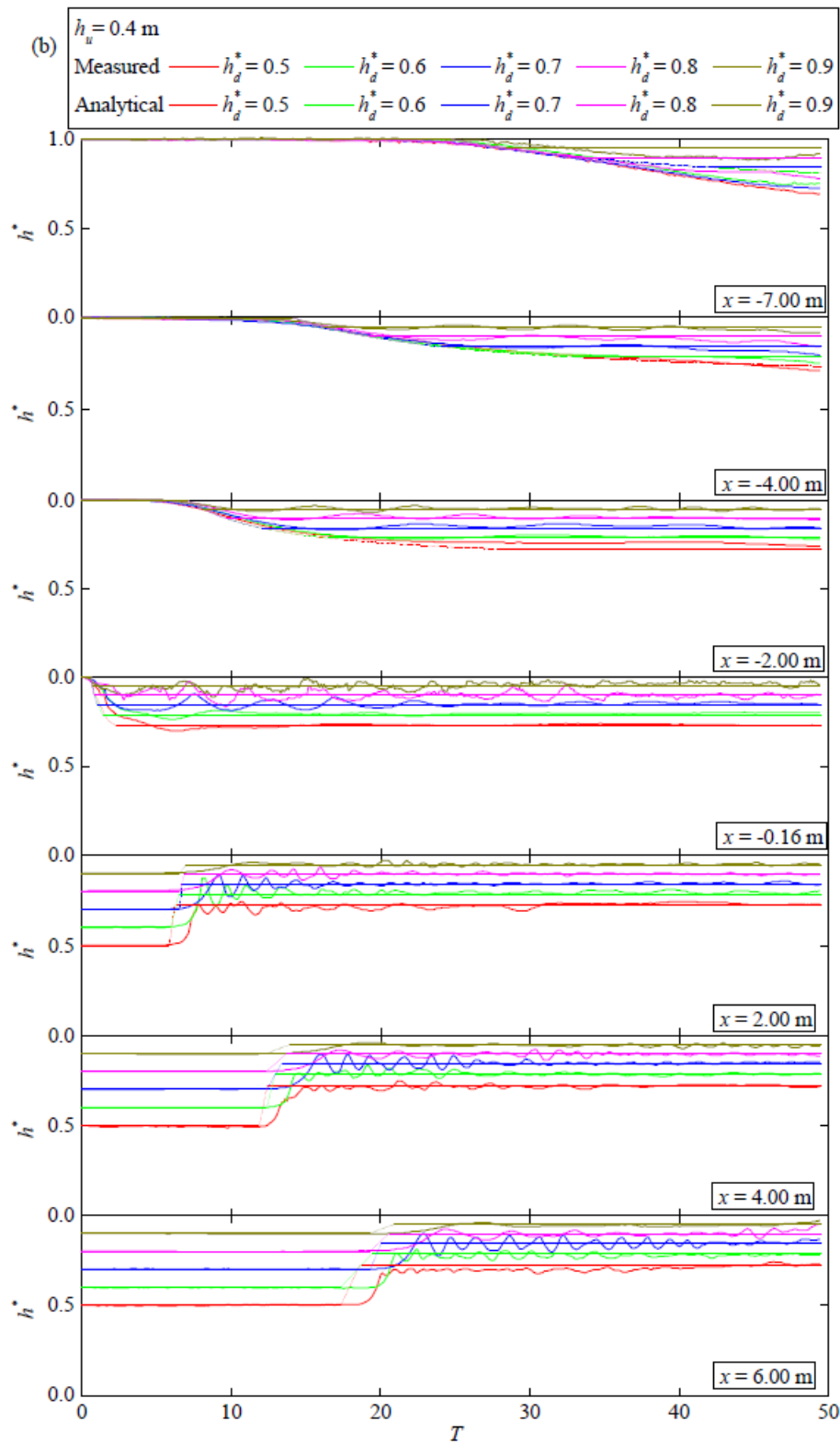
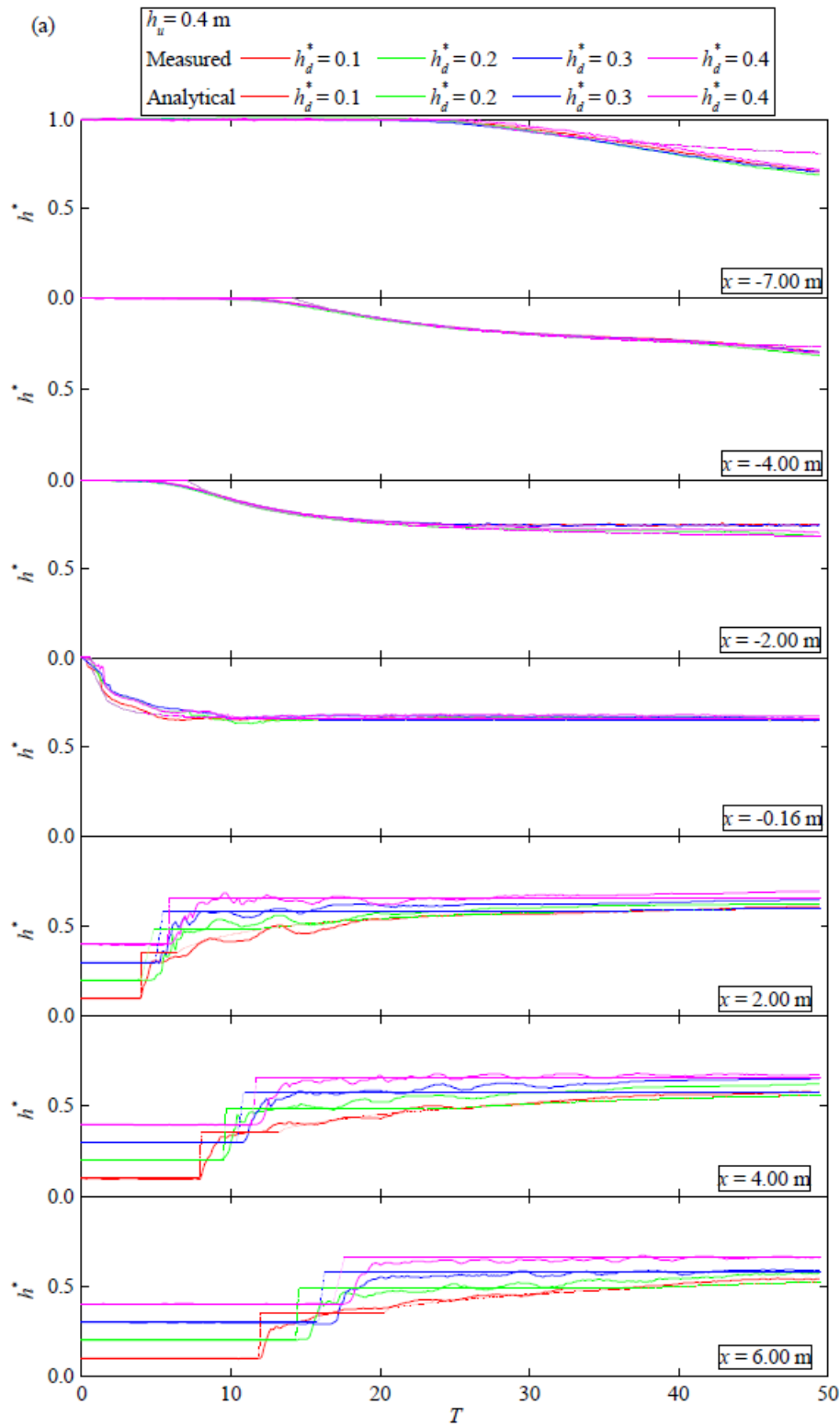


Fig. 7. Comparison of the measured and analytically predicted stage hydrographs at different positions with  $h_u = 0.4$  m for (a)  $h_d^* = 0.1, 0.2, 0.3$  and  $0.4$ ; (b)  $h_d^* = 0.5, 0.6, 0.7, 0.8$  and  $0.9$ .



728

729

730

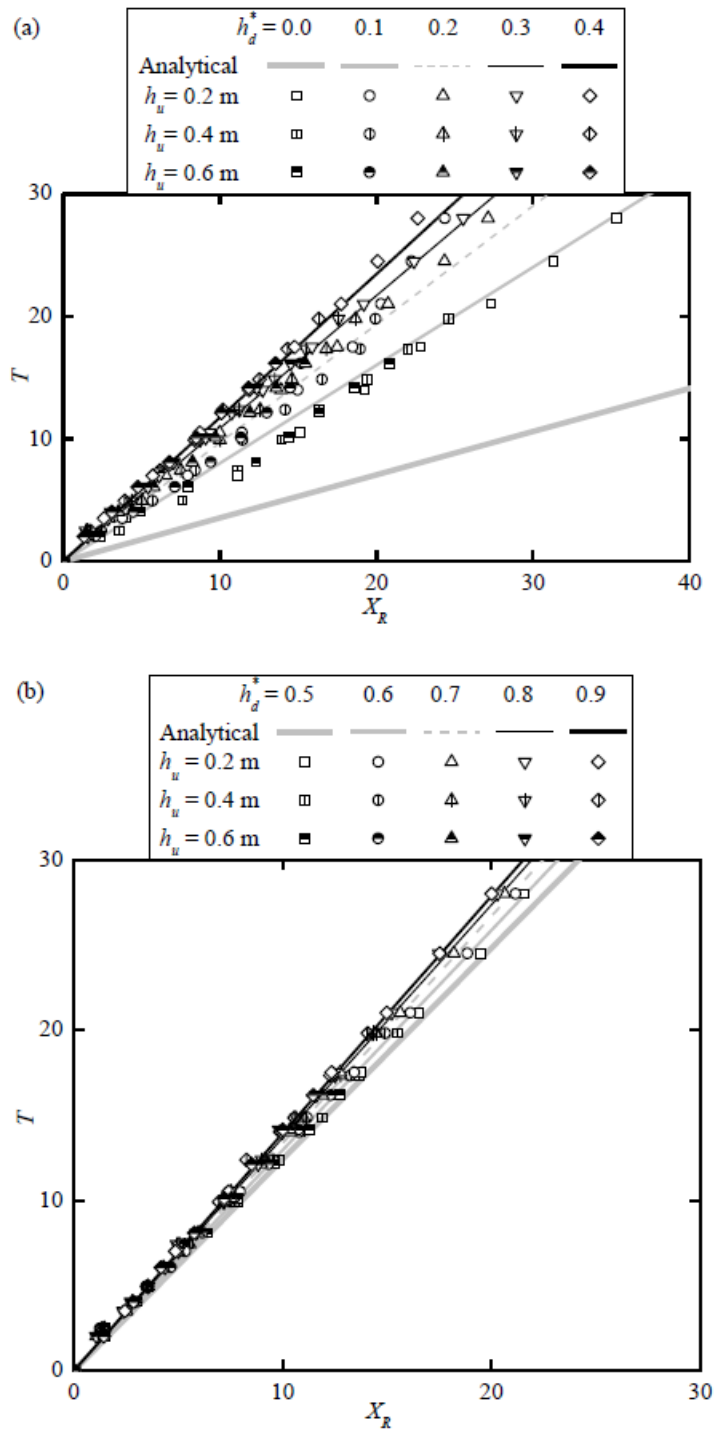


Fig. 8. Comparison of the measured and predicted locations of shock wave fronts.

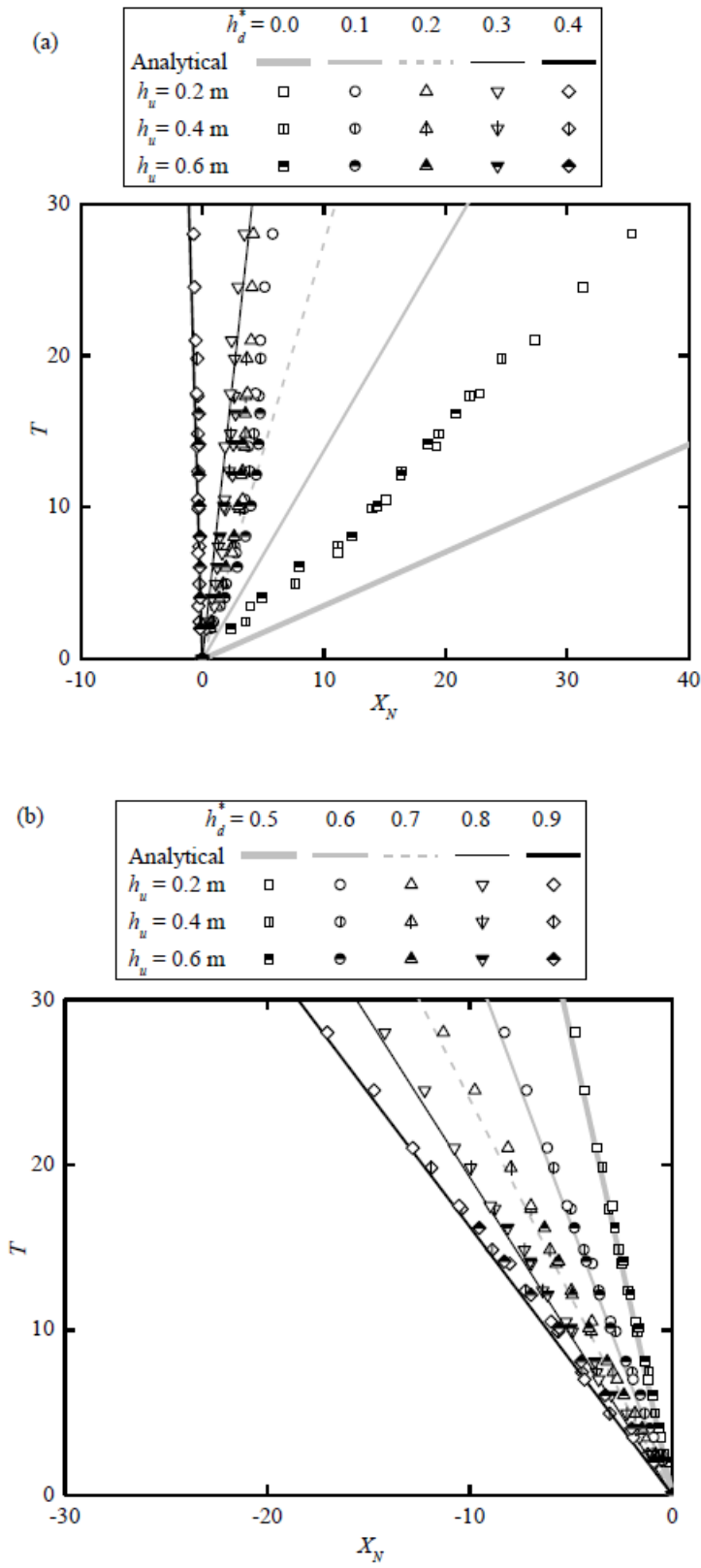


Fig. 9. Comparison of the measured and predicted locations of rarefaction wave tails.

732

733

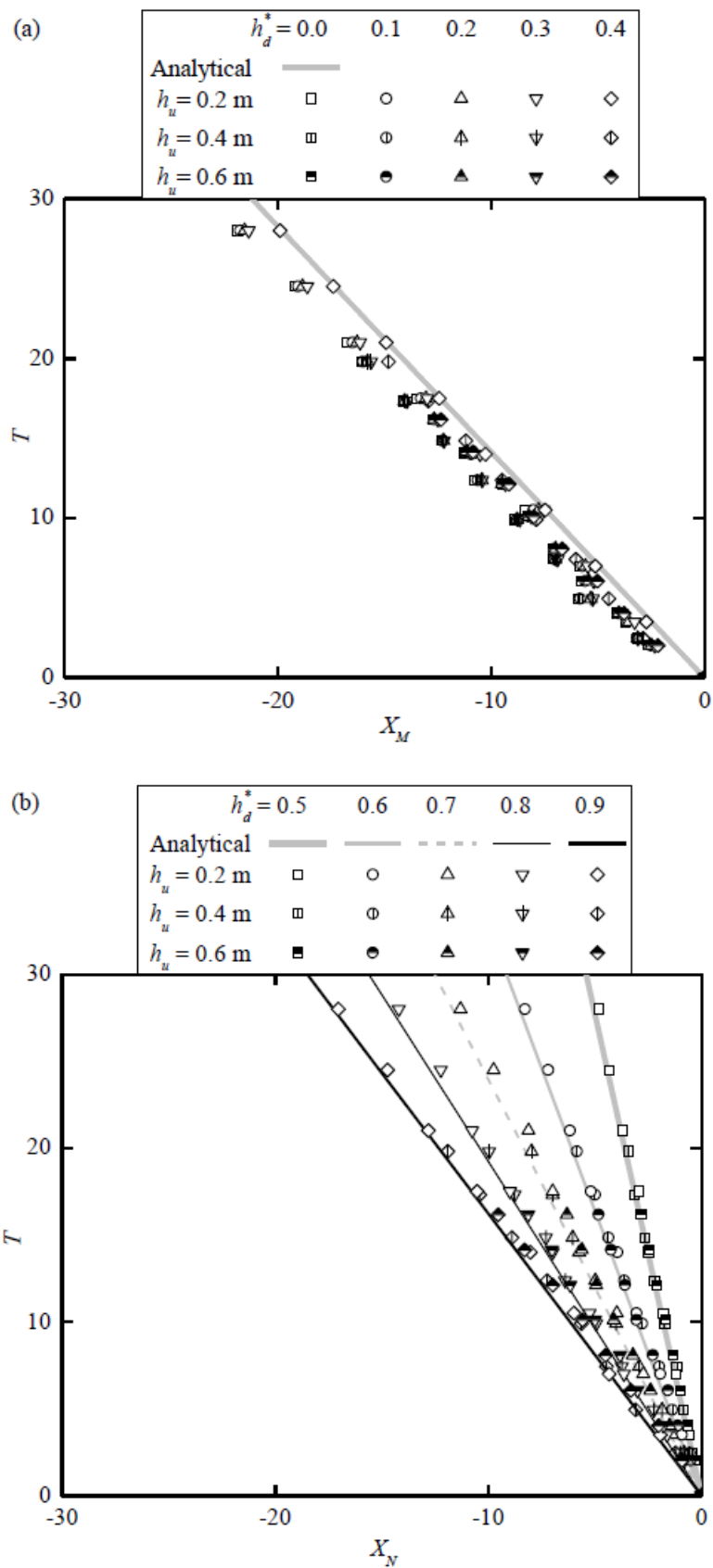


Fig. 10. Comparison of the measured and predicted locations of rarefaction wave fronts.

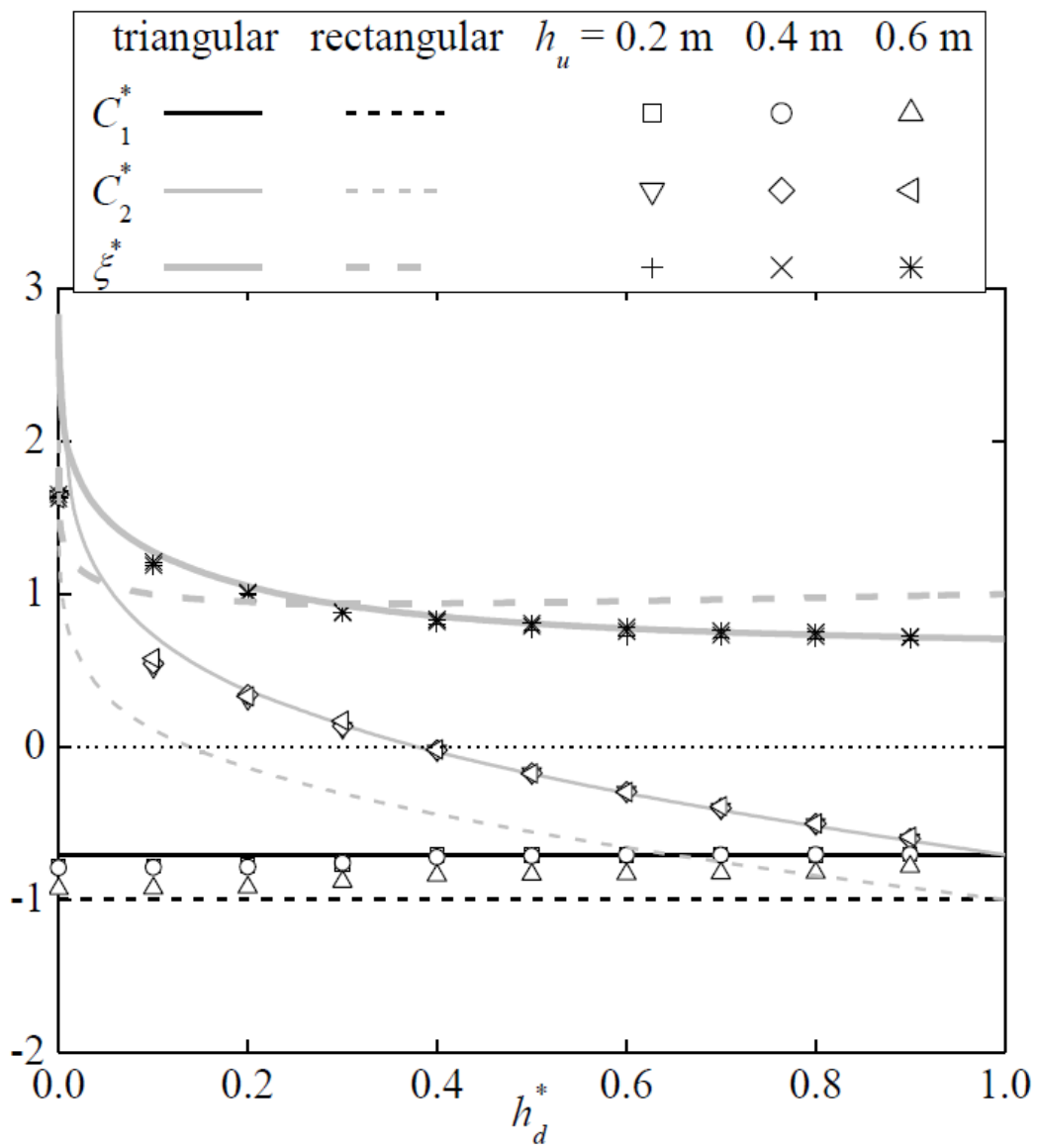


Fig. 11. Comparison of the measured and predicted  $C_1^*$ ,  $C_2^*$  and  $\xi^*$ .